

TONI TUOMINEN

Missing Baryons
and the Large-Scale Structure
of the Universe



TONI TUOMINEN

Missing Baryons
and
the Large-Scale Structure of the Universe



UNIVERSITY OF TARTU
Press

This study was carried out at Tartu Observatory, University of Tartu, Estonia.

The Dissertation was admitted on January 26th, 2023, in partial fulfillment of the requirements for the degree of Doctor of Philosophy in physics, and allowed for defense by the Council of the Institute of Physics, University of Tartu.

Supervisor: Dr. Jukka Nevalainen,
Tartu Observatory, University of Tartu,
Tõravere, Estonia

Opponent: Prof. Emer. Mauri Valtonen,
Department of Physics and Astronomy, University of Turku,
Turku, Finland

Defense: March 10th, 2023, Tartu Observatory, University of Tartu, Estonia

ISSN 1406-0302 (print)
ISBN 978-9916-27-135-3 (print)
ISSN 2806-2132 (pdf)
ISBN 978-9916-27-136-0 (pdf)

Copyright Toni Tuominen, 2023

University of Tartu Press
www.tyk.ee

CONTENTS

List of original publications	7
List of acronyms and terms used	8
Introduction	9
1 Background	11
1.1 Baryons	11
1.1.1 Observing baryons	11
1.2 The Cosmic Web	16
1.2.1 Filaments	20
1.2.2 Heating mechanisms in filaments	21
1.2.3 Ions of the cosmic web	22
2 Data and methods	24
2.1 Hydrodynamical simulations	24
2.1.1 EAGLE	25
2.1.2 Metals and ions in simulations	25
2.2 Galaxy surveys	29
2.2.1 Sloan Digital Sky Survey - SDSS	29
2.2.2 4-metre Multi-Object Spectroscopic Telescope - 4MOST	30
2.3 Filament finding methods	30
2.3.1 Bisous	30
2.3.2 NEXUS+	32
2.4 Classification of filaments	32
2.4.1 Luminosity density field	34
3 Results	35
3.1 Missing baryons in cosmic filaments	35
3.1.1 Capturing missing baryons with filament finding methods	35
3.1.2 Luminosity density as a tracer of the missing baryons .	38
3.1.3 High LD filaments	40
3.2 O VII as a tracer of the missing baryons	41
3.2.1 Radial density profiles	42
3.2.2 Metal volume fractions and mass distributions within filaments	46
3.3 O VII column density maps	47
4 Discussion and conclusions	49
References	52

Summary in Estonian	56
Acknowledgements	57
Attached original publications	59
Curriculum vitae	116
Elulookirjeldus	119

LIST OF ORIGINAL PUBLICATIONS

This thesis is based on the following publications:

- I **Tuominen, T.**, Nevalainen, J., Tempel, E., Kuutma, T., Wijers, N., Schaye, J., Heinämäki, P., Bonamente, M., & Ganeshaiah Veena, P. 2021, *An EAGLE view of the missing baryons*, *Astronomy & Astrophysics*, 646, A156
- II Holt, P., **Tuominen, T.**, Nevalainen, J., Bonamente, M., Kuutma, T., Heinämäki, P., Tempel, E. 2022, *The scaling relation between galaxy luminosity and WHIM density from EAGLE simulations with application to SDSS data*, *Monthly Notices of the Royal Astronomical Society*, Volume 513, Issue 3
- III **Tuominen, T.**, Nevalainen, J., Heinämäki, P., Tempel, E., Wijers, N., Bonamente, M., Aragon-Calvo, M., & Finoguenov, A. 2023, *Cosmic metal invaders: intergalactic O VII as a tracer of the hot WHIM within cosmic filaments in the EAGLE simulation*, *Astronomy & Astrophysics*, accepted for publication

Author's contribution to the publications

The Author has made considerable contributions to the following original publications. The following list gives details on the author's work in each of the papers. The Roman numerals correspond to those in the list of publications.

Publication I. The author performed most of the calculations and analysis, made most of the figures and wrote a most of the text.

Publication II. The author prepared the simulated and observational data, and was significantly involved throughout the process of the analysis.

Publication III. The author analysed the simulation data, made most of the figures, and wrote most of the text.

LIST OF ACRONYMS AND TERMS USED

AGN - active galactic nucleus
CDDF - column density distribution function
CIE - collisional ionisation equilibrium
DM - dark matter
EAGLE - Evolution and Assembly of GaLaxies and their Environments simulation
 H_0 - Hubble constant
H_I - neutrally charged hydrogen
IGM - intergalactic medium
LD - luminosity density
LSS - large-scale structure
Mpc - megaparsec, 10^6 parsecs, 10^{24} centimetres
 M_r - absolute luminosity in r -band
 M_\odot - mass of the Sun
FUV - far ultra-violet
SDSS - Sloan Digital Sky Survey
tSZ - thermal Sunyaev-Zel'dovich effect
WHIM - warm-hot intergalactic medium
 z - cosmological redshift
 Λ CDM - Lambda cold dark matter, concordance cosmology with a cosmological constant and cold dark matter
Å - angstrom, 10^{-10} metres

INTRODUCTION

Since the dawn of time, we have tried to understand the world around us. What lies beyond the trees, beyond the mountains, beyond the seas, beyond the stars. Now, while we know more than ever before, we understand better than ever before how little we know. A clear example of this is the matter-energy content of the Universe: the ordinary matter amounts only to $\sim 5\%$. Dark matter is expected to fill $\sim 26\%$ of the Universe, yet its nature keeps eluding us. Even more mysterious is the dark energy ($\sim 69\%$ of the matter-energy content), forcing the Universe to expand at an ever-accelerating speed (as far as we currently understand). But in addition to these enigmatic and unknown elements, in the local Universe we are missing half of the ordinary matter as well. From all the matter and energy content in the local Universe, we can directly observe less than 2.5% !

Since the late 1990's, this issue has been known as the missing baryons problem. The fraction of baryons in the Universe is very well constrained by *Planck* observations of the density fluctuations in the cosmic microwave background (CMB). However, despite several attempts to ascertain the cosmic baryon mass budget contained within different astrophysical structures, such as stars, galaxies and gas, every census has fallen short by $30\% - 50\%$.

The question of the missing baryons is the main problem tackled in this thesis. Earlier works with simulations have suggested that the missing baryons reside within cosmic filaments, in a state of warm-hot intergalactic medium (WHIM). The diffuse nature of this WHIM makes observations challenging, as it requires extremely sensitive instruments, at the very limit of our technical capabilities. Moreover, WHIM observations are generally carried out in the far ultra-violet (FUV) and X-ray bands. Since (luckily for life) our planet's atmosphere absorbs radiation in these wavelengths, instruments must be placed onboard space telescopes. Naturally, the limits on size and weight for sending instruments to space further hinder their ability to detect weak absorption or emission systems. Given the difficulties, it is essential to devise methods to optimise observational projects.

The main aims of this doctoral work were to first characterise the hot intergalactic medium, and subsequently study the feasibility of using the O VII ion absorption to trace these missing baryons. The rationale for using O VII comes from the temperatures of the hot WHIM. At $\log T(K) = 5.5 - 7$, elements lighter than Oxygen are nearly completely ionised, rendering them virtually invisible. On the other hand, at these temperatures O VII is the dominant Oxygen ion. Thus, assuming a spatial collocation of the missing baryons and the O VII ions, it is possible to infer the amount of missing baryons within the cosmic web by measuring the density of the intergalactic O VII.

In order to circumvent the observational challenges, to achieve our goals we used the modern hydrodynamic simulation EAGLE. Given that previous works predicted that the WHIM is located within cosmic filaments, we applied filament finding methods to the simulated data. These methods are algorithms created to detect the filamentary pattern of the cosmic web. While the filaments are often easily detectable by eye, a proper characterisation of the cosmic web is not straightforward. Thus, a wide range of methods have been developed, most commonly using galaxies or matter density fields to trace the large-scale structure. While a number of methods are focused on the filaments alone, some are designed to detect other features of the large-scale structure as well. These are the nodes, dense concentrations of gas and galaxies, walls, tenuous planar structures surrounding the voids, which are low-density regions almost devoid of galaxies and gas.

The filament finding methods applied in this work were the Bisous and NEXUS+. Whereas Bisous uses galaxies to trace the filamentary network, we used NEXUS+ with the dark matter density field to detect all the different components of the cosmic web. Since neither of the methods were designed to trace the intergalactic medium, any result obtained using these filament finders would be, to some extent, independent from the method. A positive correlation between the filaments and the hot WHIM would, indeed, aid significantly in the search of the missing baryons. Moreover, if the filaments are found to be filled with O VII ions, the next generation of X-ray instruments ought to be able to trace the hot gas within filaments via the ionised Oxygen.

This thesis is divided into four different chapters. Chapter 1 gives an overview of the scientific background, describing the current observational and theoretical status of both the missing baryons and the cosmic filaments. Chapter 2 describes the simulation, observational data and different methods used in the publications. Chapter 3 presents a comprehensive overview of the key results obtained in the published papers. Finally, Chapter 4 states the main conclusions and challenges, and takes a look into the future.

CHAPTER 1

BACKGROUND

During the final decade of the last century it became increasingly obvious that something was missing. Attempts to derive the baryon budget in the local Universe from different observations kept falling short of the total cosmic baryon budget (e.g. Fukugita et al. 1998). Finally, the question of the missing baryons gained traction with the consequential work of Cen & Ostriker (1999), titled *"Where are the baryons?"*. In their work, the authors ran a large-scale simulation to obtain an understanding of where the missing baryons could be found. They concluded that a significant fraction of the baryons reside in the intergalactic medium (IGM), in an ionised and diffuse state within cosmic filaments (see Fig. 1.1). Understanding this warm-hot intergalactic medium (WHIM) and producing predictions to aid in the search of it are the main goals of this thesis.

1.1 Baryons

The term baryon is used as an umbrella expression to describe all of the ordinary matter, from which stars, planets and ourselves are made of. Specifically, in the standard model of particle physics, a baryon is a particle composed of an odd number of quarks, such as protons and neutrons (three quarks each). Thus, every atom in the Universe is composed of both baryons and electrons, with neutral Hydrogen having one of each. However, when studying the mass content of the Universe, it is convenient to consider only the baryons due to their large mass: a proton is 10 000 times more massive than an electron. Ultimately, the sum of all the baryons within atoms as well as free baryons equals to the total mass of the ordinary matter in the Universe.

1.1.1 Observing baryons

In order to observe the baryons, they must interact with light. This is obvious when looking around us. We see things (i.e. baryons) as they interact with light in the visible part of the spectrum. In a similar way, different instruments can be used to detect baryons interacting with light at different frequencies of the spectrum, from radio up to gamma-rays. Ideally, one should be able to infer the baryon content in the Universe by observing baryonic systems throughout the spectrum. The total baryon content could then be computed by summing together the baryon fractions from individual contributions.

Several such baryon budgets have been calculated for different redshifts, revealing the baryon distribution at different moments in the evolution of the

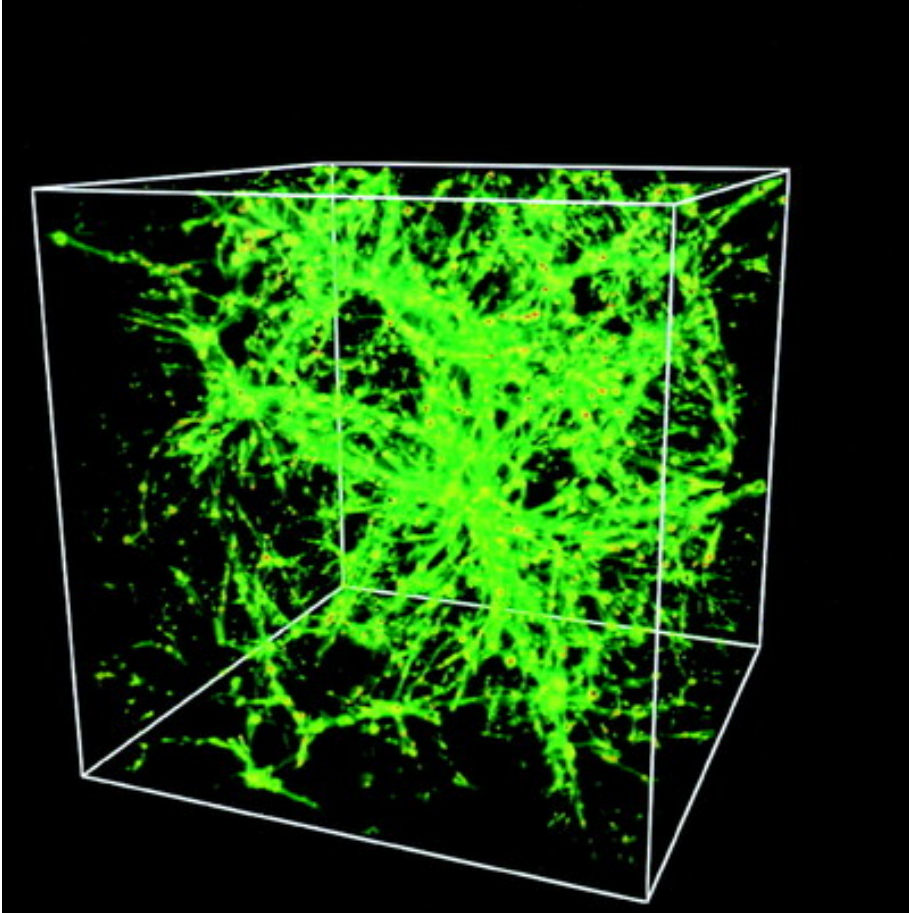


Figure 1.1: Simulation output showing the distribution of the WHIM filling the large-scale structure of the Universe. Source: Cen & Ostriker (1999).

Universe (e.g. Persic & Salucci 1992; Fukugita et al. 1998; Shull et al. 2012, and references therein). The baryonic matter in galaxies can be computed from the luminosity of their stars, together with signatures of dust and gas in their spectra. Gas around galaxies in groups and clusters is often dense enough to emit radiation, thus being readily observable. Absorption signatures in bright background sources can also reveal intervening structures (see Fig. 1.2 for an example of X-ray absorption within filaments). At higher redshifts the IGM is observed through Lyman α absorption, as Hydrogen clouds are ionised by background radiation. This gives a baryon content in agreement with CMB observations and theories of Big Bang Nucleosynthesis (BBN).

In the low redshift Universe, however, a significant fraction of the IGM has been heated to very high temperatures, within the range of $\log T(K) = 5 - 7$ (see Section 1.2.2 for the heating of the WHIM). These extreme temperatures have caused the baryons to be in a state of ionised plasma. Almost all of the Hydrogen and Helium, the two most common elements in the Universe, have lost their electrons, becoming virtually invisible or leaving only weak absorption signals in the spectra of bright background sources. However, heavier elements are able to retain their electrons and can act as proxies to trace the bulk of the baryons. For determining the baryon content through the observed density of metal ions we must know what portion these ions take from the total baryon density. For this, we need to estimate the ion fraction (i.e. what fraction of the element is in the observed state of ionisation) as well as the metallicity, that is, the ratio between the observed element and Hydrogen. Neither of these requirements are easily met. In addition, the extremely low density of the intergalactic medium makes it very challenging to detect the absorption signals. The warm phase of the WHIM ($\log T(K) = 5 - 5.5$), has been successfully traced by ions in the UV range, such as C IV (three times ionised Carbon) or O VI (five times ionised Oxygen), and thermally broadened Lyman α absorption (e.g. Danforth et al. 2016). The hot phase ($\log T(K) = 5.5 - 7$), however, has proven more challenging to detect, as the ions are on the X-ray range (see Fig. 1.3 for an example of an O VII absorption signature). While background active galactic nuclei (AGN's) remain bright in X-rays, their intensity is much lower than at the UV range, requiring the X-ray ions to have higher column densities. Only a handful of detections have been reported, many of which tentative (see Nevalainen et al. 2019; Nicastro et al. 2022, for reviews on recent observations). This observational challenge has rendered the hot WHIM mostly undetected, making it a good candidate for the missing baryons.

While absorption signals from individual absorbers remain scarce, Kovács et al. (2019) obtained a statistically significant O VII absorption signal by stacking the observed spectra with itself. This was achieved by assuming co-existence of O VII with prior UV ion detections by Tripp et al. (1998). The observed X-ray spectra was shifted according to the known redshifts given by

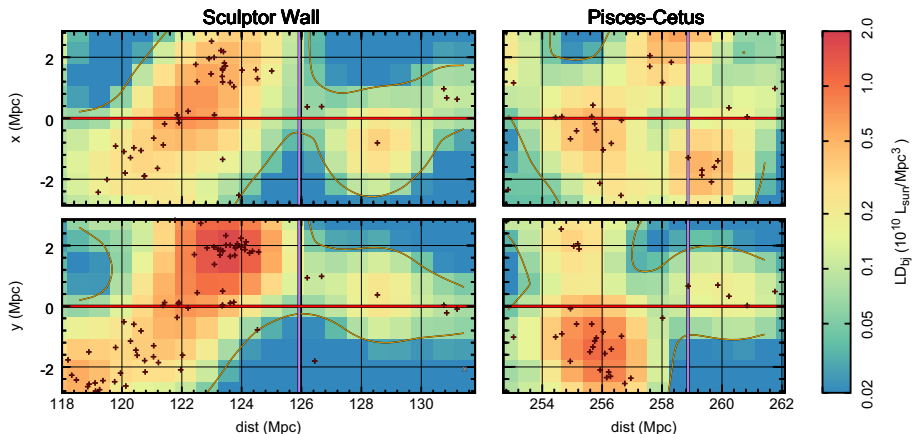


Figure 1.2: Line of sight towards the blazar H2356-309 (red horizontal lines), with the perpendicular purple lines indicating the locations of two *Chandra* X-ray absorption lines (Zappacosta et al. 2010; Fang et al. 2010). The colour scheme indicates the luminosity density field (LD, see Section 2.4.1 for a description) for 1.4 Mpc thick slices around the line of sight in two orthogonal directions (x and y). The contours indicate a LD limit of $LD_{b_j, min} = 0.05 \times 10^{10} L_{\odot} \text{Mpc}^{-3}$. Plus signs are filamentary galaxies. Source: Nevalainen et al. (2015).

the UV systems, and subsequently stacked to reveal an absorption line at the O VII wavelength.

In addition to detecting the IGM through absorption, it is possible to observe it via emission or the thermal Sunyaev-Zel'dovich (tSZ) effect. The tSZ relies on the free electrons in the plasma. The CMB radiation passing through a hot plasma experiences inverse Compton scattering, with photons receiving energy from the free electrons. The observed CMB spectra then shows a displacement towards higher frequencies, revealing the direction of the intervening plasma (the tSZ is redshift independent, it does not reveal the distance to the gas). Assuming that the tSZ signal originates from filaments, Tanimura et al. (2020a) compared the Compton y map from the *Planck* collaboration (Planck Collaboration et al. 2016b) with the filament catalogue created by Malavasi et al. (2020). By stacking the Compton y map at the positions of the filaments they were able to detect a previously unobserved tSZ signal, indicating that the filaments indeed are filled with hot plasma.

Emission, on the other hand, works in an opposite manner to absorption: photons are emitted from the intergalactic metals. While it does not require a background source, the WHIM densities are so low that for individual systems the emission is more challenging to detect than the absorption. Indeed, by stacking the same filaments as for the tSZ, Tanimura et al. (2020b) detected a statistically significant signal of X-ray emission attributed to the WHIM.

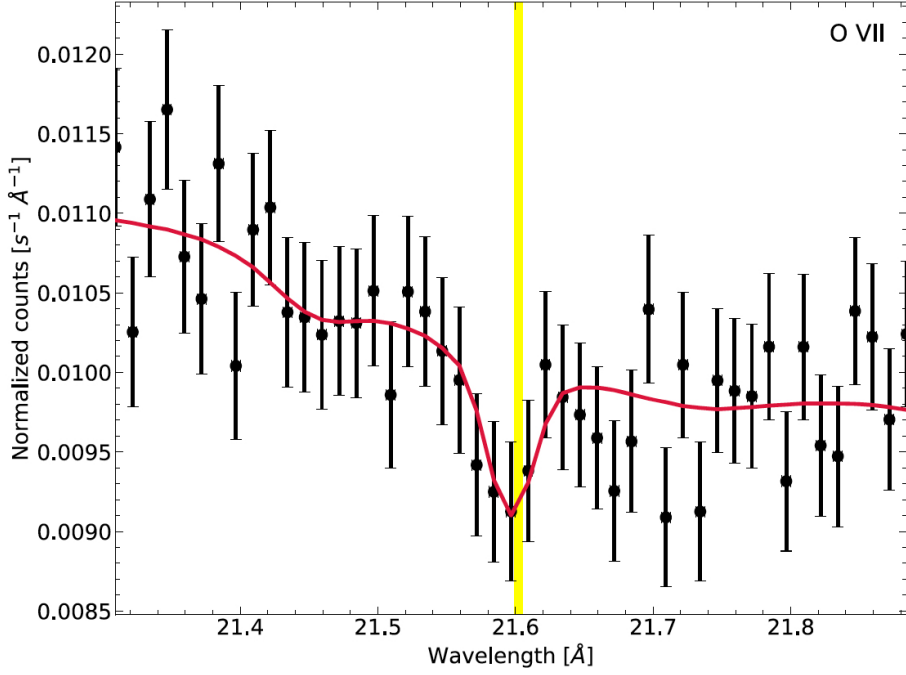


Figure 1.3: Stacked spectra of H 1821+643 around the rest-frame wavelength of O VII. The spectra was redshifted and stacked 17 times according to prior absorption line detections of UV ions. Source: Kovács et al. (2019).

Recently, Tanimura et al. (2022) used eROSITA data to detect the WHIM using only a fraction of the filaments from previous works.

Thus, currently absorption, emission and tSZ require the stacking of spectra or filaments to uncover the signal originating from the hot WHIM. This inevitably results in obtaining a mean value for the metal or electron densities, which could be biased towards low or high densities. The aim of this doctoral work was to provide observational tools and predictions to detect individual absorbing systems via X-ray detections. For this end we studied the baryons within the cosmic web using a state-of-the-art hydrodynamical simulation, EAGLE (described in Section 2.1.1).

1.2 The Cosmic Web

The baryons described above are not randomly distributed in the Universe. On large scales, they follow a complex pattern of clusters, filaments, sheets and voids, known as the cosmic web (e.g. Jöeveer & Einasto 1978; Bond et al. 1996). Clusters are dense concentrations of gas and galaxies, filaments are elongated strands connecting clusters, sheets are tenuous walls of baryons dividing voids, which are large, empty regions that fill most of the volume of the Universe (see Fig. 1.4). On the largest scales, this pattern is expected to be homogeneous and isotropic, meaning that matter is distributed uniformly and symmetrically across all directions. In other words, changing the position of the observer would not change the geometry and matter distribution of the observed Universe. These are the basic assumptions upon which rests the standard cosmological model, the Lambda Cold Dark Matter (Λ CDM) model. The model describes the observed Universe from soon after the Big Bang until the present time (albeit with some caveats). At present time, the Universe is dominated by dark energy ($69.2\% \pm 1.2\%$ of the energy content Universe), a non-zero vacuum energy described with the cosmological constant Λ , and dark matter ($25.9\% \pm 1.2\%$ of the Universe), an unknown substance that interacts with baryons and radiation only through gravity (Planck Collaboration et al. 2016a). The remaining $4.84\% \pm 0.04\%$ are the baryons we are (ideally) able to directly observe. Notably, the small errors are an indication of how well these values are constrained by the *Planck* observations.

As the evolution of the cosmic web is driven by the gravitational collapse of initial density perturbations, it is dominated by the dark matter. Moreover, as dark matter does not interact with radiation, it started immediately forming structures. During the first $\sim 380\,000$ years the Universe was dominated by radiation, and interactions with photons kept the baryons in a hot, ionising plasma. Thus, when baryons finally decoupled from radiation, their structure formation was enhanced by the pre-existing potential wells of the dark matter, leading to the large-scale structures we observe today. At the same time, the Universe became optically thin, allowing photons to travel freely. This last

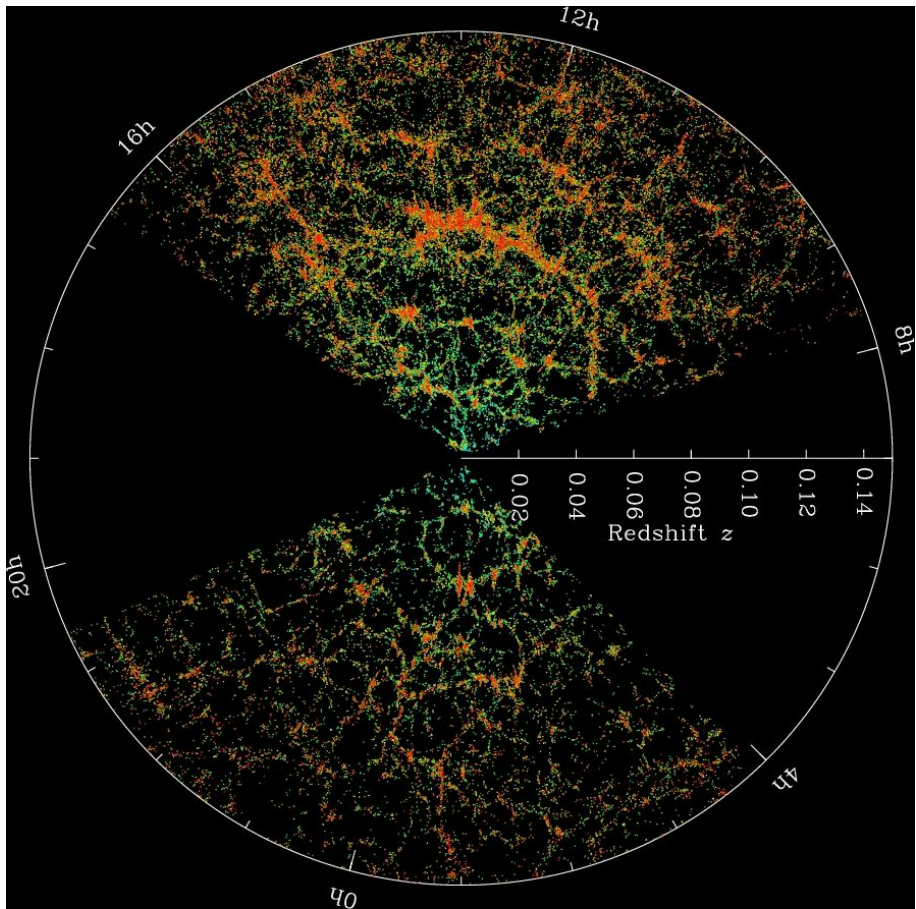


Figure 1.4: The cosmic web, as observed by the SDSS galaxy survey. Each dot is a galaxy, showing the $g - r$ colour of that galaxy. The two black areas are shaded by the plane of our own galaxy. Image Credit: M. Blanton and SDSS (<https://www.sdss.org/>).

scattering surface is the cosmic microwave background (CMB) we observe today.

Perturbations in the matter (both dark and baryonic) density field can be described with a dimensionless density contrast δ :

$$\delta(\mathbf{x}) = \frac{\rho(\mathbf{x})}{\bar{\rho}} - 1, \quad (1.1)$$

where \mathbf{x} are the co-moving coordinates of the perturbation with density $\rho(\mathbf{x})$, and $\bar{\rho}$ is the mean density of the Universe. At present time, the mean baryon density of the Universe corresponds to $\bar{\rho}_b = 6.18 \times 10^9 M_\odot/\text{Mpc}^3 = 4.41 \times 10^{-31} \text{g/cm}^3$, where M_\odot is the solar mass. The mean density is sometimes expressed in terms of Hydrogen number density, $n_H = 1.88 \times 10^{-7} \text{cm}^{-3}$.

Given the assumptions on homogeneity and isotropy, at large scales the structure formation can be described with a fluid approximation. Moreover, the initial conditions of this fluid are well approximated by a Gaussian random field, which can be characterised by its power spectrum:

$$P(t, k) \propto k^{n_s}, \quad (1.2)$$

with t being time, k the wave number and n_s the spectral index of the power law. The effectiveness of the power spectrum is that, in the linear regime, the power spectrum at any given time can be related to the initial power spectrum via a (model dependent) transfer function. And the initial power spectrum, in turn, can be derived from CMB observations, which give it a spectral index of $n_s = 0.968$ (Planck Collaboration et al. 2016a). What the power spectrum represents, in essence, is the amount of structure within a given scale $\lambda \simeq 2\pi/k$. This is explained by the fact that the power spectrum is the Fourier transform of the two-point correlation function of the density field, defined as:

$$\xi(x) = \langle \delta_1 \delta_2 \rangle, \quad \text{where } x = |\mathbf{x}_1 - \mathbf{x}_2|. \quad (1.3)$$

As ξ is dependant only on the distance between two perturbations, it probes the scales of the most prominent perturbations. These perturbations, imprinted in the CMB, evolved to form the large-scale structures we observe today, dominated by the dark matter (see Figure 1.5 for the dark matter distribution in the EAGLE simulation). This evolution can also be described with the power spectrum, using a model-dependant transfer function.

However, once the local density contrast approaches unity $\delta \sim 1$ (i.e $\rho \sim 2\bar{\rho}$), the evolution of the perturbations begins to deviate from the linear regime. At this point, analytical description of the structure formation is no longer straightforward. Indeed, at present time clusters, filaments and sheets are all in the non-linear regime.

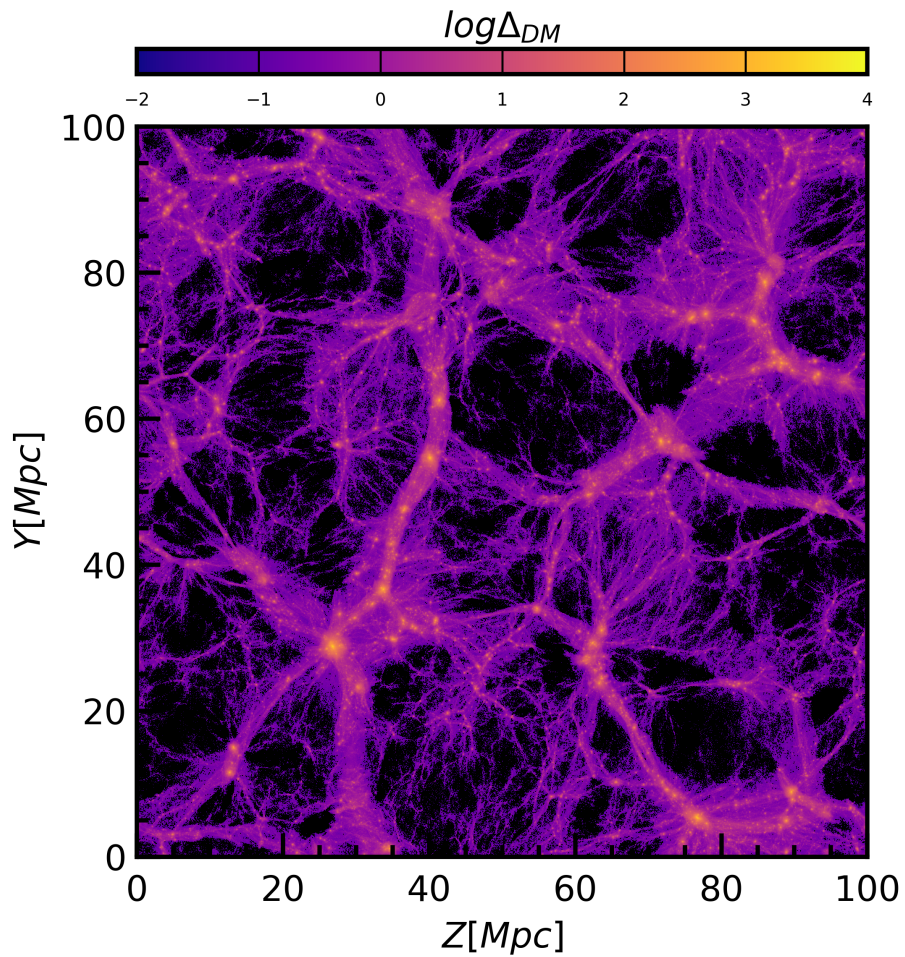


Figure 1.5: Projection of the dark matter density within the EAGLE simulation, in a 5 Mpc thick slice. The colour scale is presented in terms of density contrast $\Delta = \delta + 1 = \rho/\bar{\rho}$.

Structures like galaxies, groups and clusters can be characterised by the virial theorem: gravitation-driven spherical collapse is halted by internal pressure, resulting in hydrostatic equilibrium. Collapsed structures can be identified by their virial radius, defined as the boundary within which the density is 200 times the critical density, i.e. $\rho_{\text{virial}} = 200\rho_c$. The critical density is given by $\rho_c = 3H^2/8\pi G$, the density of a flat, matter-dominated universe (Einstein-de Sitter model).

Still, most of the baryons reside in the intergalactic medium, beyond the virial radius of collapsed structures. While densities within groups and clusters of galaxies are high, observational evidence suggests that the intra-cluster medium (ICM) contains only approximately 4% of the baryon budget (Shull et al. 2012). This can be explained by the very small volumes they cover, $< 1\%$ of the total volume (computed from cosmological simulations, Cautun et al. 2014; Ganeshaiah Veena et al. 2019). On the other extreme, Ganeshaiah Veena et al. (2019) found that voids and sheets cover $\approx 94\%$ of the volume, but only $\approx 45\%$ of the baryon gas. While some of this gas is contained within isolated galaxies, the bulk of it is in the form of very diffuse and cool gas, observable via photoionised and broadened $\text{Ly}\alpha$ absorption (Shull et al. 2012). The remaining half of the baryons are located in the filaments, in the form of warm-hot intergalactic medium. Since the observational status of the WHIM, especially the hot phase, is unresolved, focusing on filaments is essential in the search for the missing baryons.

1.2.1 Filaments

Filaments are some of the most prominent features of the Universe, criss-crossing through space for lengths of up to a hundred Megaparsecs. While visually identifiable from the spatial distribution of galaxies (that trace the underlying dark matter density field), they are challenging to quantify analytically. The well-defined linear perturbation theory is only applicable to the isotropic growth of structures for a density contrast of $\delta \ll 1$. Filaments, being overdense, are a natural outcome of the non-linear anisotropic evolution of the cosmic web, driven by gravitational collapse. But they are not virialised structures such as clusters are. Thus, they cannot be explained by the spherical collapse model, and large-scale tidal fields have to be taken into account (Zel'dovich 1970; Cautun et al. 2014). The original seeds of the cosmic web can be detected in the CMB as small density fluctuations, which are subsequently amplified by gravitational processes as the Universe evolves. Following the Zel'dovich approximation (Zel'dovich 1970), the structures of the cosmic web can be described by the eigenvalues of the deformation tensor in the tidal field. While collapse occurs simultaneously in all directions, the pace of the collapse is different. Thus, the following simplification is valid to describe the evolution of the large-scale structure. First, structures collapse unilaterally

(along one dimension) to form a sheet, with one positive eigenvalue. Then, collapse occurs along a second dimension to form a filament, with two positive eigenvalues. Finally, collapse along the third dimension will result in a spherical structure, with three positive eigenvalues.

However, proper identification and description of the filaments remains challenging, despite the reliable idea of perturbation growths in the cosmic web given by the Zel’dovich approximation. This difficulty arises from the filament’s fractal, multi-scale nature, as well as the complex interaction of the different environments of the cosmic web. Some thick and short filaments (or bridges) connect nearby clusters, while long filaments reach lengths of 100 Mpc, and small tenuous tendrils transport gas from the filaments into the haloes. Thus, in practice, filaments are detected in a wide variety of methods. For a comparison of a wide range of properties obtained with several filament finding tools, see Libeskind et al. (2018). The filament finding methods used in this work are the Bisous (Stoica et al. 2007, 2010; Tempel et al. 2016b) and MMF/NEXUS+ (Aragón-Calvo et al. 2007; Cautun et al. 2013), described in detail in Section 2.3.

1.2.2 Heating mechanisms in filaments

The missing baryons reside in cosmic filaments in a state of warm-hot intergalactic medium, at temperatures of $\log T(K) = 5 - 7$. But how did the IGM get heated to such high temperatures? This heating is mainly driven by shocks formed by the infall of baryons from sheets and voids into filaments (e.g. Cen & Ostriker 1999; Ryu et al. 2003; Kang et al. 2005). As gas experiences the gravitational pull of the underlying dark matter distribution, it accretes towards regions of higher densities. As the density increases, the accretion becomes supersonic and creates a shock with very high Mach numbers, $M \sim 10 - 100$. Furthermore, within filaments this gas experiences additional shocks by further accretion of the shocked gas, mergers and chaotic supersonic flow motions. While these inner shocks have low Mach numbers, the mean shock speed is larger than for external shocks. The energy of both internal and external shocks is dissipated into the IGM, increasing its temperature. At the very low densities of the WHIM, the cooling times exceed the Hubble time, thus retaining the energy generated by the shocks.

In addition to shocks, the filament gas is heated by supernova and AGN feedbacks. While both feedback effects play a secondary role compared to the shock heating, AGN feedback may induce extra heating of the WHIM as well as displace gas from haloes back to the IGM. Using the SIMBA simulation, Bradley et al. (2022) compared the effects of AGN feedback in the thermodynamic properties of the IGM. They found that by turning on the AGN feedback, the fraction of WHIM of the total baryon content increased from $\sim 30\%$ to $\sim 70\%$. This, however, did not result in higher column densities for the metal ions permeating the WHIM, indicating that the metallicity did not increase.

1.2.3 Ions of the cosmic web

Given that the filamentary gas is shock-heated to temperatures of $\log T(K) = 5 - 7$, most of the neutral Hydrogen and Helium are completely ionised. As described in Section 1.1.1, highly ionised metals can be used as proxies for tracing the bulk of the baryons. In particular, O VII is the dominant ion at the hot WHIM temperatures, $\log T(K) = 5.5 - 7$, assuming collisional ionisation equilibrium (CIE, Mazzotta et al. 1998). In purely CIE conditions and temperatures around $\log T(K) \sim 6$, almost all of the Oxygen is ionised to O VII. However, the low densities in filaments allow for photoionisation by the background UV and X-ray radiation to affect the ion fraction distributions (see Fig. 1.6). Thus, the fractions of O VI-VIII in filaments are a combination of CIE and photoionisation equilibrium, determined both by the temperature and density of the filamentary medium.

Given that the problem of the missing baryons is the result of a complex interplay between the formation and evolution of the filamentary large-scale structure, the thermodynamics of the hot ionised plasma within the filaments, as well as the chemistry and physics of Hydrogen, Helium and metals, this work relies on a wide range of tools and methods to bring everything together. These methods are described in detail in the following chapter.

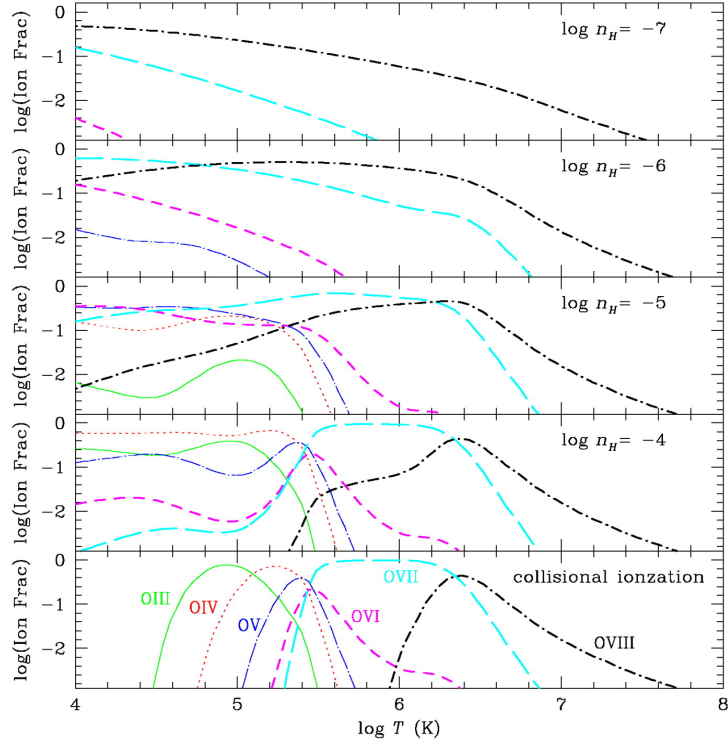


Figure 1.6: Ionisation fractions of Oxygen as a function of temperature for different baryon densities, given by the Hydrogen number density $\log n_H$. Source: Kang et al. (2005).

CHAPTER 2

DATA AND METHODS

The reason a significant fraction of the baryons has been missing is most likely of an observational nature: our instruments are not sensitive enough to detect the hot and diffuse intergalactic medium. However, simulations can be used to circumvent the observational challenges and infer some properties of the WHIM. While limited by their mass resolution, they are a powerful tool to build a theoretical base of the thermodynamic properties of the IGM. In simulating the large-scale structure they cover such a range of astrophysical processes, that it would be impossible to model analytically. Simulations also provide valuable predictions for future instruments and observations, especially as the computing power increases and they achieve larger cosmological scales with high resolution.

2.1 Hydrodynamical simulations

A hydrodynamical simulation follows both the evolution of the dark matter as well as the baryons. The key difference between the two matter components is that the dark matter only interacts gravitationally, both with itself and baryons. Baryons, in addition to gravity, experience self interaction, with a wide range of thermodynamic processes changing the nature of the gas, and how it further interacts with its environment. Moreover, baryons interact with photons, and for a hydrodynamical simulation to be successful it has to account for different radiative and photoionising processes. These mechanisms, in addition to being arduous to model, are computationally expensive, and for a long time failed to reproduce many key properties of galaxies we observe. Thus, until the middle of the last decade, most cosmological simulations contained only dark matter. Simulations such as the *Millenium Simulation* (Springel et al. 2005) would follow the interaction of a large number of simulation particles representing the distribution of the dark matter. After the simulation had ran its course, dark matter haloes would be identified from the dark matter distribution. Finally, galaxies were included in the simulation with semi-analytical models and halo occupation distributions (e.g. Guo et al. 2013).

However, semi-analytical models rely on simplifications and approximations. In addition, and more importantly for the work presented in this thesis, dark matter only simulations with semi-analytical models do not reproduce the intergalactic medium. Thus, with increasing computational power and refined baryonic models, hydrodynamical simulations have gained more significance. Indeed, modern hydrodynamical simulations are able to reproduce the observable galaxy properties to a high degree.

2.1.1 EAGLE

The Evolution and Assembly of GaLaxies and their Environments (EAGLE) is a suite of several cosmological simulations (Schaye et al. 2015). All the simulations are hydrodynamical, following both dark matter and baryons within periodic volumes of different sizes ranging between 25 to 100 comoving Mpc on a side. All simulations started from an initial redshift $z = 20$ and evolved until redshift $z = 0$. The largest simulation, REFL0100N1504, has a cubic size of 100^3 Mpc^3 and contains a total of 1504^3 dark matter and baryon particles. The initial mass of the dark matter and baryon particles was $m_{DM} = 9.7 \times 10^6 M_\odot$ and $m_b = 1.81 \times 10^6 M_\odot$, respectively. While individual dark matter particles maintained their mass throughout the simulation runs, the baryon gas particles were allowed to transfer mass from one particle to another, as well as to collapse into stellar and black hole particles. Via stellar feedback, some of the mass in stellar particles would return to gas particles. With this dynamic interaction, EAGLE was able to follow the formation of galaxies as well as their environments in the large-scale structure of the universe.

The suite of the EAGLE simulations were run assuming the standard model of cosmology, with a cosmological constant Λ and cold dark matter (Λ CDM model). The fractions of dark energy, dark matter and baryons used in the simulation were given by *Planck* observations as $\Omega_\Lambda = 0.69$, $\Omega_{dm} = 0.26$ and $\Omega_b = 0.048$, respectively (Planck Collaboration et al. 2014).

EAGLE was run as an N -Body simulation. In essence, in N -Body simulations a continuous field is represented by discrete simulation particles. In this way, each particle carries a wide range of properties of the volume they describe, such as temperature, density and mass. To achieve this, the simulation runs a TreePM algorithm, a combination of a hierarchical multipole expansion with a Fourier transform particle mesh (PM). The PM reduces the number of operations computed, while the hierarchical tree algorithm divides the particles into cubic shells. The resolution within each cell can then be adjusted based on the particle density, to optimise the computational resources. In addition, to model the subgrid physics for the baryon particles, EAGLE applied smoothed particle hydrodynamics (SPH). Each SPH particle was thus able to interact with its surroundings to better model the hydrodynamic effects moulding the cosmic web.

2.1.2 Metals and ions in simulations

In addition to thermodynamic properties, each SPH particle carries information on H and He fractions as well as metallicity. These metals are produced in stars within galaxies, using the subgrid physics modelled within each SPH. The metals are spread to the IGM with feedback models computing the galactic superwinds caused by supernovae. The main species of metals followed in the simulation are C, N, O, Ne, Mg, Si, S, Ca, and Fe, with an implementation

of radiative cooling and photoheating. Each SPH particle also stores the mass fraction of these elements, with particle interactions distributing metals at each simulation step. In particular, in the present work we used the smoothed metallicity abundances. Namely, the spread of metals is improved by allowing more neighbours to be contaminated. Otherwise, the spread of metals is truncated by the discrete nature of the simulation particles.

The fraction of ions within each SPH particle is computed separately. We used ionisation tables obtained with CLOUDY (Ferland et al. 1998), an algorithm to compute synthetic spectra and ionisation fractions. It combines a host of astrophysical processes to calculate for a given atom its different ionisation states for different environmental conditions (see upper panels in Fig. 2.1 for CLOUDY outputs of O VI, O VII and O VIII). Then, combining the ionisation data with the local temperature and density, it is possible to obtain the fraction of the desired ions within each SPH particle. For Paper III, we used the same CLOUDY tables computed by Wijers et al. (2019), with a UV/X-ray background described by Haardt & Madau (2001).

As described in Section 1.2.3, the fraction of O VII within filaments is a combination of collisional ionisation and photoionisation. This is visible in the upper panels of 2.1. At higher densities CIE dominates, and in the case where CIE dominates at hot WHIM temperatures ($\log T(K) = 5.5 - 7$), almost all of the Oxygen is ionised to O VII. At lower densities, on the other hand, photoionisation dominates, and the fraction of O VIII becomes larger for the hot WHIM temperatures (see also Figure 1.6 for the effect of density on the ion fractions). At the typical densities within cosmic filaments, $\delta \sim 10 - 100$ ($\log n_H \sim -6 - -5$), the ionisation is a result of the combination of collisional ionisation and photoionisation. As O VII dominates towards the higher densities, which are more readily detectable via absorption, in Paper III we focused solely on this ion.

Column densities

While in space the Oxygen ions are distributed in three-dimensional volumes, what is observed is the two-dimensional projection of these volumes on the plane of sky. This turns the number densities (cm^{-3}) into column densities (cm^{-2}). In essence, the column densities are integrated ion densities along the path of the line of sight. A given value for the detected column density can thus be the result of a smaller but denser structure, such as a galaxy group, or a diffuse but larger structure, such as a filament aligned along the line of sight.

The current limit for O VII absorption detections is given by instrument sensitivity and systematics. Currently, the best instrument is the RGS on board the XMM-Newton space telescope. In order to detect faint absorption systems, the instrument has to gather enough photons revealing a dip at the absorption wavelength. With exceptionally long exposure times, of the order of megaseconds (≈ 280 hours or 11 days), RGS reached column densities close

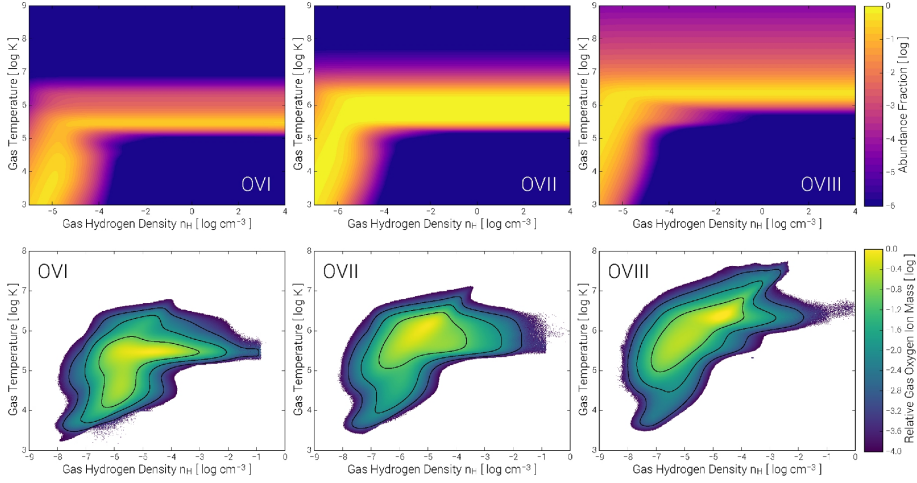


Figure 2.1: *Top panels*: Simulation independent output of CLOUDY, indicating the ionization fractions of O VI-VIII as a function of density and temperature. The horizontal regions describe the regime of predominantly collisional ionisation, while the largely vertical bands at low hydrogen number densities arise from photoionisation. *Bottom panels*: Phase diagrams of O VI - VIII mass fractions in density-temperature space for the Illustris TNG100 simulation at $z = 0$. The colour map indicates relative ion mass fractions (dark purple values at 4.0 have 10000 times less ion mass per pixel than peak pixels in yellow). The three black contours enclose relative mass log fractions of 1.0, 2.0, and 3.0, from innermost to outermost. Source: Nelson et al. (2017).

to $\log N_{\text{O VII}}(\text{cm}^{-2}) \approx 15$ (Nevalainen et al. 2017). On the side of the instrument systematics, the effective area of the instrument was calibrated with an accuracy of $\approx 2\%$ (Kaastra 2017; Nevalainen et al. 2017). Thus, a 2% spurious effect on the continuum flux could be misinterpreted as an astrophysical line with an equivalent width of a few mÅ. This, too, corresponds to a column density of $\log N_{\text{O VII}}(\text{cm}^{-2}) \approx 15$. Thus, in Paper III we adopted this as the observational limit.

With $\log N_{\text{O VII}}(\text{cm}^{-2}) \approx 15$ as the observational limit, we derived two limits for the three-dimensional O VII number densities. Considering a filament of thickness ~ 1 Mpc crossing the line of sight, to be observable the O VII density ought to be larger than $\log n_{\text{O VII}}(\text{cm}^{-3}) > -9$. On the other hand, if the line of sight to a background source travels ~ 10 Mpc within a filament, a density of $\log n_{\text{O VII}}(\text{cm}^{-3}) \sim -10$ is enough for a detection.

In order to derive observational predictions from EAGLE, we computed a set of column densities from the simulated O VII densities. As with the ion fractions, we used the same methods described in Wijers et al. (2019). In short, we divided the EAGLE box into thin and elongated columns. To compute the number of ions within each column, we distributed the ion number densities in the SPH particles to the columns they resided in. As each SPH particle represents a volume in space, we used the same smoothing kernel of the SPH algorithm to spread the ions to adjacent columns. Once the number of ions was calculated within each column, it was divided by the area of the base of the columns to obtain the two-dimensional column densities.

The length of each column was determined by the expected spectral resolution of the next generation X-ray instrument, X-IFU, onboard the future Athena space telescope. For a photon energy of ~ 0.5 keV, the energy resolution of X-IFU is 2.5 eV. This, in turn, corresponds to a redshift resolution of $\Delta z \approx 0.005$, or ≈ 20 Mpc. Thus, we divided the EAGLE simulation into five, 20 Mpc thick slices. Each slice was then divided into the aforementioned columns. The area of the base of each column was 31.25^2 kpc^2 , small compared to the column length but large enough to contain enough SPH particles even in lower density regions.

A column with a density above the observational limit is considered an absorber. A common method to quantify the number of absorbers is to use the column density distribution function (CDDF), defined as:

$$f(N, z) \equiv \frac{\partial^2 n}{\partial \log N \partial z}. \quad (2.1)$$

Here n is the number of absorbers, integrated over the column densities N and absorption paths z . The CDDF was used in Paper III, see Figure 11 for O VII column densities in different environments within the EAGLE simulation.

2.2 Galaxy surveys

Galaxies are the most obvious tracers of the cosmic web. Readily observable (when bright enough), they can be used to reconstruct the underlying filamentary network. In all three Papers we made use of the results of the Sloan Digital Sky Survey, with a look to the future with predictions for the 4-metre Multi-Object Spectroscopic Telescope in Paper III.

2.2.1 Sloan Digital Sky Survey - SDSS

Our aim when using simulations was to test models and predictions to be applied to observations. While next generation X-ray instruments are still far in the future, we can use existing galaxy surveys and filament catalogues to test our results. Currently, the most comprehensive spectroscopic galaxy survey is the Sloan Digital Sky Survey (SDSS; York et al. 2000). It started routine operations in 2000, and has since observed approximately 1/3 of the sky, with the latest public data release expected to be published in January 2023. Currently, the main telescopes carrying out the observations are the dedicated Sloan foundation 2.5m telescope at Apache Point Observatory (APO) in New Mexico, USA, and the Irénée du Pont telescope at Las Campanas observatory in Chile. The spectrographs mounted on the telescopes are the BOSS and APOGEE-1 and APOGEE-2 spectrographs. While the APOGEE spectrographs will be used to study the Milky Way, BOSS continues to observe galaxies.

In the present work we used the public data release DR12 (Alam et al. 2015). It contains the sky plane positions and redshifts of over two million galaxies. The Bisous filament finding method had previously been applied to SDSS galaxies from this and previous data releases (e.g. Tempel et al. 2014a, 2016a; Kuutma et al. 2020). The filaments were detected from a volume limited sample with a distance cut at redshift $z \approx 0.05$, corresponding to a depth of ≈ 215 Mpc. To avoid the Local Void, an underdense region surrounding our Milky Way, a lower limit of ≈ 85 Mpc was applied to the galaxy catalogue. Thus, the total radial depth of the Bisous filament catalogue is ≈ 130 Mpc, somewhat larger than the EAGLE simulation size.

In order to make our results obtained from the EAGLE simulation comparable to existing observations, we used the same criteria for obtaining the Bisous filaments in the simulation as were used for SDSS. Namely, we applied a magnitude cut to the EAGLE galaxies such that the number density of galaxies, the main property determining Bisous filaments, would be the same as in the survey. While the magnitude limit corresponding to the volume-limited sample in SDSS was $M_r = -19$, for EAGLE we settled on $M_r = -18.4$. The reason for this was that the luminosity distribution of EAGLE galaxies drops faster than the observed ones (see Figure 2 in Paper I). Therefore, the

higher magnitude limit assured that the number density was the same in both the simulation and observations.

2.2.2 4-metre Multi-Object Spectroscopic Telescope - 4MOST

In order to produce meaningful predictions for future instruments, we also considered a larger survey still under development at the time of writing. The 4-metre Multi-Object Spectroscopic Telescope (4MOST, de Jong et al. 2019) is a wide-field spectroscopic facility aimed at providing large and deep surveys of the southern sky. One community survey in particular, the 4MOST Hemisphere Survey of the Nearby Universe (4HS), will extend the depth of a complete galaxy survey up to $z = 0.15$ (i.e. ~ 600 Mpc) with a similar quality to the SDSS sample at $z = 0.05$.

2.3 Filament finding methods

As described in Section 1.2.1, defining filaments is not a straightforward task. Thus, a wide range of filament finding methods have been developed in the last decade. Libeskind et al. (2018) used simulations to describe and compare 12 different methods, with very different ways to detect filaments. Some followed the distribution of haloes or galaxies as tracers of the underlying dark matter distribution, while others relied on the velocity or density fields of the dark matter. The main difference between the methods was in the probability distribution function (PDF) of the density within volume cells in the detected filaments. The median density spans almost an order of magnitude and the shape of the PDF is similar only between similar methods (i.e. tracing haloes or the dark matter density field). On the other hand, all methods agree that a significant fraction of matter is located within filaments, while they fill a relatively small volume of the simulation. In this sense there is a slight convergence between the different methods, but in the end, each method is designed to answer a different question and is better suited for that particular task.

In Paper I we used both the Bisous as well as the NEXUS+ filaments, described in more detail below. In Papers II and III only Bisous was used.

2.3.1 Bisous

The Bisous method is a marked point process to detect filaments by fitting and aligning cylinders in regions of galaxy overdensities (Stoica et al. 2007, 2010; Tempel et al. 2014b, 2016b). Originally designed to analyse random spatial patterns, it was developed to use on galaxies to detect the large-scale filamentary pattern. Assuming that there are more galaxies within filaments than outside, the method computes the number of galaxies within cylindrical volumes. It then aligns consecutive cylinders to detect structures larger than the cylinder

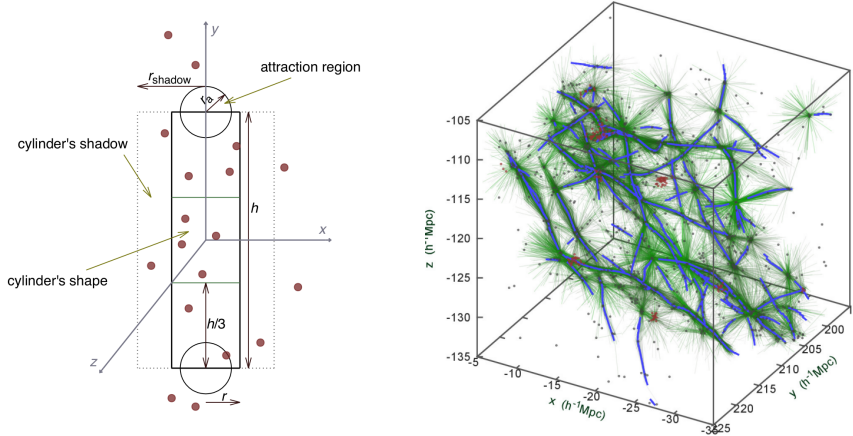


Figure 2.2: Visualisation of the Bisous filament finding method. The left-hand image shows a schematic of the how Bisous fits cylinders along galaxy overdensities (Tempel et al. 2016b). The image on the right presents the result of the Bisous method used on SDSS galaxies (Tempel et al. 2014b). Each dot is a galaxy, while each green line is one run of the Bisous method. The blue lines are the final, detected filament spines.

length. The process is repeated many times (1000 in our case) to account for its stochastic nature. The result is a three-dimensional map of the regions covered by the Bisous cylinders, and combining each individual run creates a visit map indicating the regions most often covered by the cylinders. This map is stored in a three-dimensional grid, with each grid point containing the value of the visit map in that location. Thus, by setting a limit to the visit map value it is possible to extract the filament volumes. Moreover, the filament spines are given by the maximas of the visit map. These ridges indicate the location of the backbones of the filaments. In order to remove possible spurious spines, we set a minimum limit of 2 Mpc for a spine to be considered a filament. The output, finally, is a combination of filament volumes in a three-dimensional grid, and spines, represented by a trail of consecutive points.

From all the environments in the cosmic web, Bisous is designed to detect only the filaments. While clusters have large numbers of galaxies, there is no preferred direction to align consecutive cylinders. On the other hand, walls are planar structures, not properly traceable by fitting cylinders. However, the structures we were interested in the study of the missing baryons are the filaments, for which Bisous is optimal. Moreover, since Bisous only requires galaxies as points to trace the filamentary network, it is very convenient to apply it both to simulations and observations. Thus, Bisous was our preferred filament finding method.

2.3.2 NEXUS+

To assess the systematics that arise from using filament finding methods, ideally we would compare as many methods as possible. In our work, in addition to Bisous, we used NEXUS+ (Cautun et al. 2013). Whereas Bisous relies on galaxies as points tracing the filaments, NEXUS+ works with the morphology of the density field deformation tensor, or Hessian, to detect the nodes, filaments and walls of the cosmic web (see Fig. 2.3). Following the idea behind the Zel’dovich approximation (see Section 1.2.1), it uses the eigenvalues of the Hessian matrix to assess each environment.

As a tool to study the morphology of the large-scale structure, NEXUS+ is based on the multiscale morphology filter (MMF), developed by Aragón Calvo (2007). As the name suggests, it addresses the multiscale nature of the cosmic web. As such, NEXUS+ is able to detect filamentary structures of different scales at once, from dense and hot bridges to more tenuous tendrils. To achieve this, a Gaussian filter with a given smoothing scale is first applied to the density field. In the second step, the Hessian matrix eigenvalues $\lambda_1 \leq \lambda_2 \leq \lambda_3$ are computed for the smoothed field. Thirdly, using the eigenvalues each point in the field is assigned to a node ($\lambda_1 \approx \lambda_2 \approx \lambda_3 < 0$), filament ($\lambda_1 \approx \lambda_2 < 0, \lambda_2 \ll \lambda_3$) or wall ($\lambda_1 \ll \lambda_2, \lambda_1 < 0$). Any point that is not assigned to an environment is considered to be in a void.

In the next step, the three previous steps are repeated for a range of smoothing scales. By combining the outputs from all scales, the result is a scale-independent signature of the large-scale structure. Finally, a detection threshold based on physical criteria is used to determine the valid structures.

NEXUS+ can be applied to any density field, such as baryon or galaxy number density. Since the large-scale structure is dominated by the dark matter, we applied the NEXUS+ method to the EAGLE dark matter density field.

2.4 Classification of filaments

Filaments reside in a variety of environments. Some filaments contain more gas and galaxies, while other are tenuous trails of gas with very few galaxies. At the same time, filaments can vary in length between just a few Mpc to a hundred Mpc. Indeed, Galárraga-Espinosa et al. (2020) used the length of the filaments to classify them into short and long filaments. This was done using two hydrodynamical simulation, the Illustris-TNG (Nelson et al. 2019) and MAGNETICUM¹, while the filaments were detected using DisPerSe (Sousbie et al. 2011). They found that shorter ($< 9\text{Mpc}$) filaments are thicker, denser and connected to more massive structures than longer ($> 20\text{Mpc}$) filaments, concluding that they are intrinsically different objects.

¹www.magneticum.org

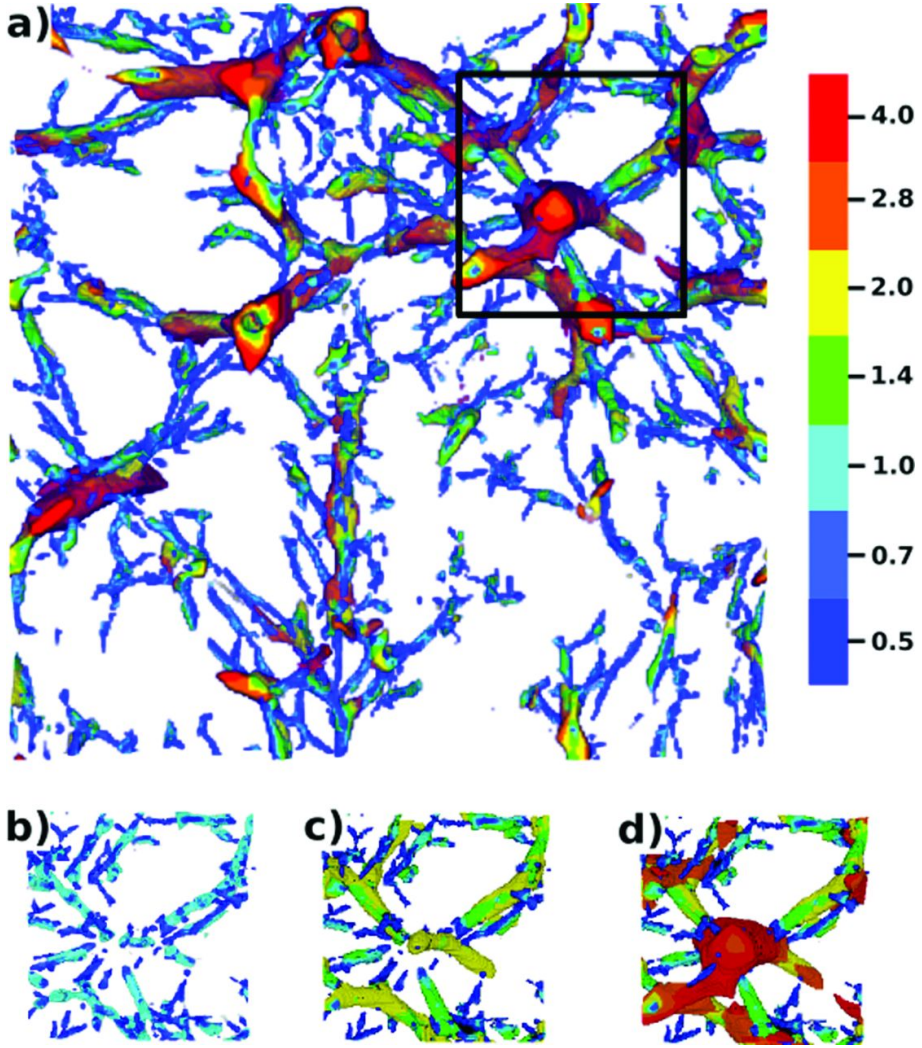


Figure 2.3: Filaments detected with the NEXUS+ within an N -body simulation. Different colours indicate the smoothing scale that gives the largest filamentary signature for a given volume, in units of $h^1\text{Mpc}$. A zoom-in region, indicated by the black square in panel (a), is shown in panels (b)–(d). These panels show the filaments detected using a smoothing scale with a maximum of (b) 1, (c) 2 and (d) $4h^{-1}$. Source: Cautun et al. (2013).

2.4.1 Luminosity density field

Our approach to classifying filaments relied on the galaxy luminosity density field (for a comprehensive description of the method, see Liivamägi et al. 2012). The luminosity density (LD) field is constructed by distributing the galaxies' luminosity with a given smoothing scale, forming a continuous field. Thus, the LD traces the galaxy densities, which in turn trace the underlying dark matter distribution. In this manner, the LD can be used to uncover different structures of the cosmic web. Moreover, using simulations Nevalainen et al. (2015) showed a linear correlation between the LD and the WHIM density, with higher luminosity density tracing higher baryon densities. This relation was further studied in Paper II (see Figure 8 in Paper II).

In practice, for computing the LD field we created a cubic grid with l number of points, separately for EAGLE and SDSS. The EAGLE grid consisted of a cube with 500^3 number of grid points and a step between each point of 0.2 Mpc. For SDSS, we computed grid points only within Bisous filaments. In order to maintain the same cell volumes as in EAGLE, the SDSS grid points were separated by steps of 0.2 Mpc. The density was then computed at each grid point with a kernel sum:

$$l_{\mathbf{i}} = \frac{1}{a^3} \sum_{gal} K^{(3)} \left(\frac{\mathbf{r}_{gal} - \mathbf{r}_{\mathbf{i}}}{a} \right) L_{gal}, \quad (2.2)$$

with \mathbf{i} denoting the grid indices $\mathbf{i} = (i_1, i_2, i_3)$, $\mathbf{r}_{\mathbf{i}}$ being the coordinates of the grid point \mathbf{i} and \mathbf{r}_{gal} the coordinates of each galaxy used for the field. L_{gal} is the galaxy luminosity which, for observations, is multiplied by a weight factor that accounts for the extinction caused by distance. To distribute the luminosity from point sources (galaxies) to a continuous field, a three-dimensional kernel function $K^{(3)}$ is applied, with a smoothing scale a .

The smoothing was done using a one-dimensional B_3 spline kernel. It resembles a Gaussian distribution, but with the wings cut at a distance of $2a$ from the peak, i.e. the function is non-zero only within the range $[-2a, 2a]$. The three-dimensional kernel was then computed as a product of three one-dimensional kernels.

To classify the filaments based on their environment, we evaluated the luminosity density field at the filament spine points with a smoothing scale of $a = 2$ Mpc. Then, computing the mean luminosity density of each spine we divided them into low, medium and high luminosity groups.

In addition to using the LD for classifying filaments, in Paper II we studied the relation between WHIM and luminosity densities to derive a scaling relation between the two.

CHAPTER 3

RESULTS

This Chapter presents an overview of the results from the published papers. The results can be divided into two categories: the baryon distribution and thermodynamic properties within cosmic filaments, and the observational prospects of O VII as a tracer of the filamentary baryons.

3.1 Missing baryons in cosmic filaments

The first objective was to confirm previous simulation results with the EAGLE simulation. In particular, to assess whether a significant fraction of baryons reside in the hot WHIM phase ($\log T(K) = 5.5 - 7$), and whether these WHIM baryons indeed are within cosmic filaments. A first view of the simulation seems to support these assumption (Figs. 3.1 and 3.2). Intergalactic baryons are distributed along seemingly filamentary structures, where the gas reaches temperatures above $\log T(K) > 7$.

Nevertheless, a simple projection is not enough to determine the content of the hot WHIM within EAGLE. Thus, in Paper I we computed the mass fraction contained within every SPH particle outside any virialised structures, that is, all baryons outside R_{200} . In addition, we selected only those particles with temperatures above $\log T(K) > 5.5$. The amount of this hot, intergalactic gas comprises 29% of the total baryon budget in the simulation. This means that approximately one third of all the baryons reside in a diffuse intergalactic phase, at temperatures that render them very challenging to observe. When compared to the baryon census carried out by Shull et al. (2012), the fraction of hot WHIM in EAGLE is strikingly similar to the fraction of missing baryons (both are $\approx 29\%$).

3.1.1 Capturing missing baryons with filament finding methods

As described above, approximately one third of the baryons within EAGLE are in a hot and diffuse state, seemingly within cosmic filaments. But since they are challenging to detect, how could we tap into these baryons in observations? Our approach was to test whether filament finding methods could be used to capture them.

For Paper I, we ran both Bisous and NEXUS+ methods on EAGLE galaxies and the dark matter density field, respectively (see Section 2.3 for a description of these methods). We found that for WHIM temperatures ($\log T(K) = 5 - 7$) most of the baryons are within filaments (Figure 12 in Paper I). Moreover, both filament finding methods agree well (within 10%) on the baryon

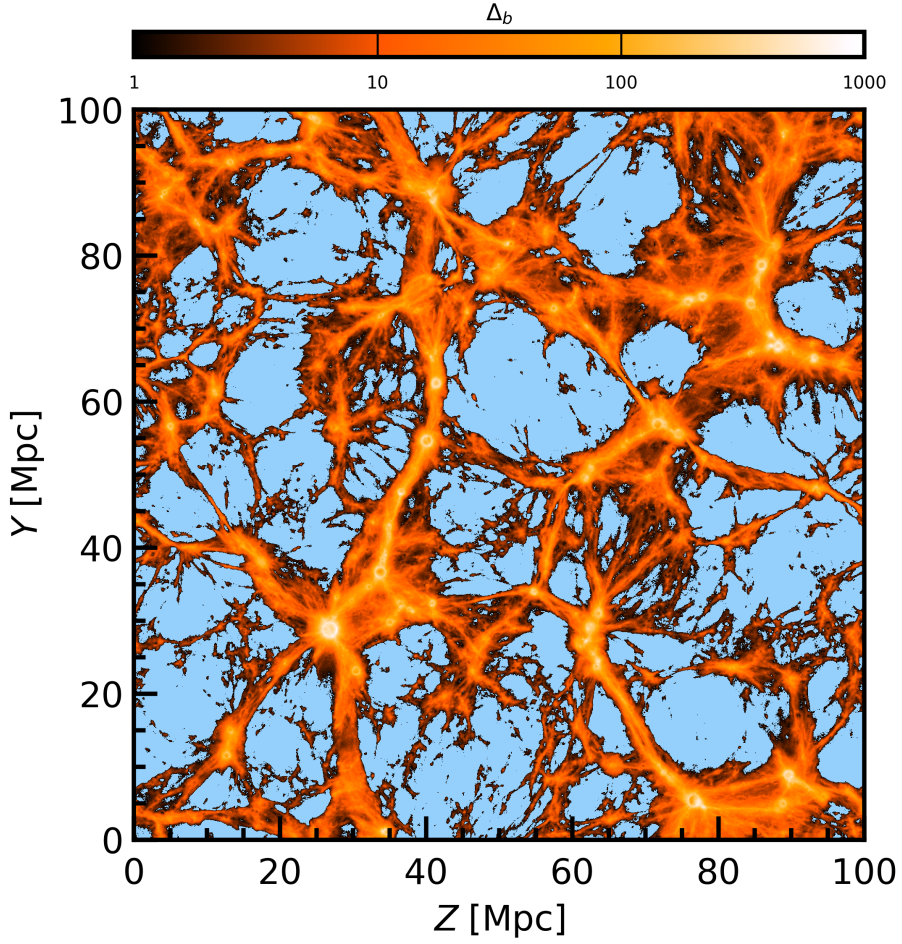


Figure 3.1: Projection of the intergalactic baryons in the EAGLE simulation within the same slice as in Figure 1.5. All gas within R_{200} has been removed. The colour scale corresponds to baryon overdensities, with underdense regions (below mean cosmic density) shown in blue.

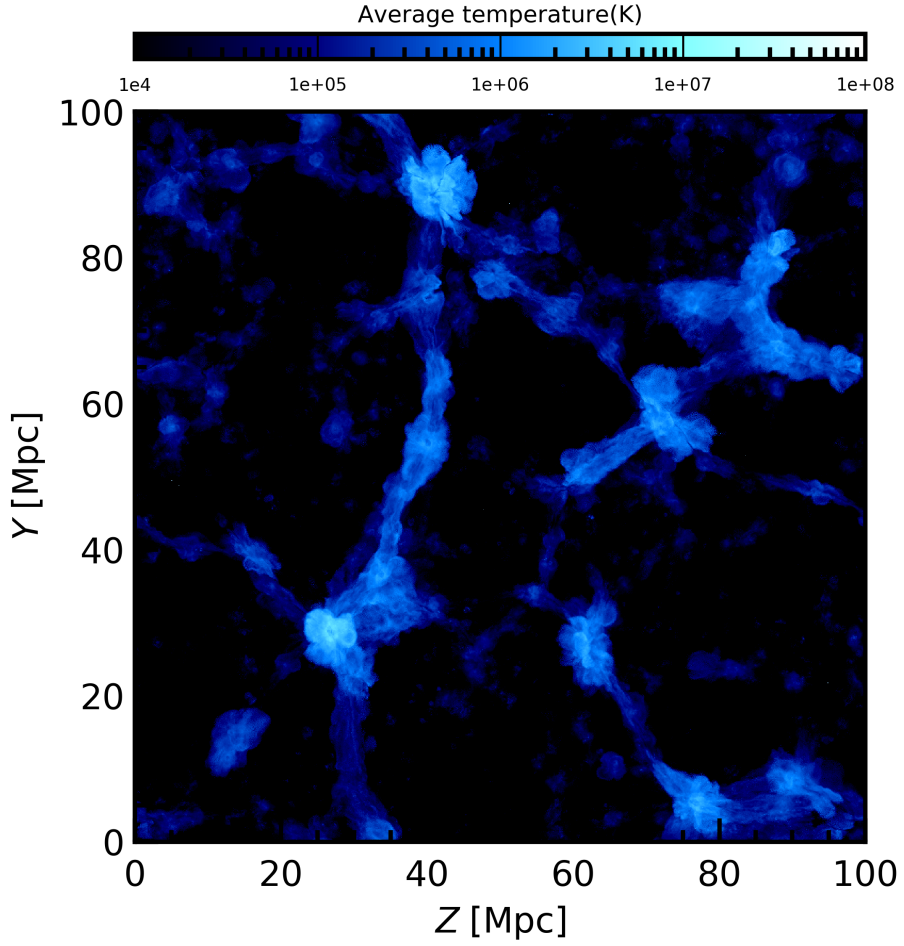


Figure 3.2: Same 5 Mpc thick slice as in Figures 1.5 and 3.1, but with a projection of the average temperature of the intergalactic baryons. All gas within R_{200} has been removed. The colour scale corresponds to baryon temperatures.

content at those temperatures. Bisous filaments contain slightly more baryons than NEXUS+ on both the low and high temperature ends of the WHIM temperature range. This can be explained by the main difference between the two methods: Bisous is designed to find only the filaments, while NEXUS+ detects also walls and nodes. Thus, part of the baryons within Bisous filaments are within NEXUS+ walls (at lower temperatures) or nodes (at higher temperatures).

From all the hot WHIM baryons, $\approx 87\%$ are contained within Bisous and $\approx 79\%$ within NEXUS+ filaments. The difference can be explained by the overlap of Bisous filaments with NEXUS+ walls and nodes described above. Taking that into consideration, in Paper I we concluded that both Bisous and NEXUS+ agree well, and a significant fraction of the hot WHIM is contained within filaments detectable by different methods. Thus, the captured fraction of hot WHIM (i.e. missing baryons) within these filament finding methods is $\approx 25\%$ of all the baryons within the simulation.

However, filaments contain intergalactic gas in a variety of thermal states. Indeed, of all the IGM within Bisous filaments, the fraction of hot WHIM is $\approx 63\%$. Therefore, nearly half of the baryons within filaments are not in the state of hot WHIM, and cannot be considered missing. Thus, a strategy had to be devised to select the optimal filaments, with the highest content of missing baryons.

3.1.2 Luminosity density as a tracer of the missing baryons

Driven by gravity, the formation of the cosmic web is dominated by dark matter. All the baryons, including both galaxies and the diffuse IGM, follow this large-scale structure. Moreover, most of the baryons reside in cosmic filaments, both in virialised structures as well as in the diffuse extragalactic medium. Thus, it is to be expected that the galaxy luminosity could be able to trace the IGM to some extent. In particular, using the luminosity density (LD, see Section 2.4.1) field, it should be possible to locate a fraction of the IGM, and by extension, of the missing baryons.

Nevalainen et al. (2015) found that, indeed, the LD can be used to trace the WHIM. Building upon this foundation, in Paper II we further analysed this relation using the EAGLE simulation. In addition, we applied the new scaling relation to SDSS data to obtain an estimate of WHIM mass within the observed filaments.

To properly study the LD–WHIM density relation, we divided the EAGLE simulation into 500^3 cells, each with a volume of $V_{cell} = 0.2\text{Mpc}^3$. Subsequently, within each cell we computed the mass-weighted mean temperature as well as the IGM density. To remove the gas particles within R_{200} of virialised structures, we computed the volume covered by each SPH particle within these structures (see equation (3) in Paper II). Thus, the IGM density was defined as

the mass of the particles outside R_{200} of any halo, divided by the volume of the cell minus the volume within collapsed structures.

In order to find the optimal smoothing scale for the LD field, we studied the linear correlation coefficient between the WHIM density and 50 LD fields with smoothing scales ranging between $a = 0.1 - 5$ Mpc (Figure 2 in Paper II). The coefficient peaks at $a = 1.2$ Mpc, indicating the optimal smoothing scale to trace most of the WHIM. At smaller scales the luminosity of galaxies does not spread far enough into the IGM, while too large smoothing scales already include WHIM-free voids.

Given the optimal smoothing scale, we derived a linear scaling relation in logarithmic space (equation (5) in Paper II):

$$\log \delta_\rho = \log A + B \log \delta_{LD}. \quad (3.1)$$

Using 10 000 Monte Carlo samples to determine the best fits for the free variables, we found that $\log A = -0.27$ and $B = 0.89$.

Knowing that the Bisous filaments are able to capture a significant fraction of the WHIM, we combined both the scaling relation given by the LD field together with the filaments. Since our tests on EAGLE gave promising results in estimating the WHIM content based on the scaling relation (see Table 5 from Paper II), we applied this method to SDSS data. We divided the SDSS volume within Bisous filaments into cells of the same size as in EAGLE, namely $V_{cell,SDSS} = 0.2\text{Mpc}^3$. Within these cells we then computed the LD with a smoothing scale of $a = 1.2$ Mpc. With the scaling relation given by 3.1 we then computed the predicted WHIM density within each cell. With the cell volumes and densities we were able to compute the WHIM mass contained in each cell (equation (6) in Paper II), and therefore within the whole SDSS volume. Finally, this gave us an estimate of the baryon fraction in the WHIM:

$$\Omega_{b,LD} = (0.31 \pm 0.07 \pm 0.12) \Omega_b, \quad (3.2)$$

where $\Omega_{b,LD}$ is the WHIM baryon fraction given by the LD relation, and Ω_b the total baryon fraction. The statistical error (± 0.07) is given by the determination of the scaling relation, while systematic errors (± 0.12) arise from the choices and estimates made during the analysis. Essentially, the computed baryon fraction reflects the amount of WHIM that is expected to reside within Bisous filaments in the SDSS volume. While it is at the lower end of the expected fraction of baryons within the WHIM (30% – 50%, see e.g. Shull et al. 2012; Danforth et al. 2016), it represents a significant portion of the total baryon budget. Notably, this value was computed within volumes of observational filament data. Stacking the tSZ signal from a different sample of SDSS filaments, Tanimura et al. (2020a) measured a baryon fraction of $\approx 8\%$ of the

total baryon budget. Given that the tSZ signal is stronger at higher temperatures and densities, it is possible that they traced the hotter counterpart of the WHIM, thus obtaining a lower value than our prediction. A confirmation to these estimates might have to wait for future X-ray instruments.

3.1.3 High LD filaments

As described in Section 2.4.1, we used the LD field to classify filaments into three distinctive groups. The filaments in the high LD group were found to contain the largest hot WHIM fraction within them. While for the whole filament sample the fraction of hot WHIM over the total baryon content within filaments is $\approx 63\%$, for filaments within high LD regions this fraction rises to $\approx 82\%$. Thus, concentrating in high LD filaments is expected to yield the best results for finding the missing baryons.

To confirm the advantage of concentrating on high LD filaments, and to further study their thermodynamic properties, we computed radial density and temperature profiles from the filament spines (see Figures 13 and 15 in Paper I). For the whole filament sample, both the median density and median temperature peak at the spines of the filaments, decreasing as a function of distance. And as expected, when computing radial profiles for the high LD spines only, the temperatures and densities are significantly higher. At the high LD spines, the median temperature is $\log T(K) \approx 6$ and median density is $\log \rho(M_\odot/\text{Mpc}^3) \approx 11.3$, or $\delta_b \approx 40$.

In order to verify the relevance of this result, we performed a null test by repeating the radial profiles on randomly rotated and displaced filament spines. This resulted on flat profiles at background temperatures ($\log T(K) \sim 3$) and densities ($\log \rho(M_\odot/\text{Mpc}^3) \approx 8.9$).

Given the regular radial behaviour of the temperature and density profiles for the high LD filament sample, we fitted a single- β model for both profiles:

$$T(r) = T_0 \times \left[1 + \left(\frac{r}{r_{c,T}} \right)^3 \right]^{(-\frac{3}{2}\beta_T)} \quad (3.3)$$

$$\rho(r) = \rho_0 \times \left[1 + \left(\frac{r}{r_{c,\rho}} \right)^2 \right]^{(-\frac{3}{2}\beta_\rho)} + bkg. \quad (3.4)$$

Here, T_0 and ρ_0 are the temperature and density at the core of the filaments, respectively. In a similar way, $r_{c,T}$ and $r_{c,\rho}$ are the core radii of the temperature and density profiles, respectively, determined by the best fit of the β models to the data.

In order to assess the reliability of our profiles, we turned to the observational results of Tanimura et al. (2020a). At the positions of a large number of DisPerSe filaments, they stacked the Compton y maps given by *Planck* observations. From the tSZ effect reflected in the y maps they computed the plasma temperatures and densities. This way they obtained radial temperature and density profiles as a function of distance from the filament spines. We found a good agreement when comparing our profiles to the ones observed by Tanimura et al. (2020a), when focusing on the central regions of the spines. Within errors, we obtained similar core temperatures and densities.

Galárraga-Espinosa et al. (2021) used the Illustris-TNG simulation and DisPerSe filaments to derive radial temperature and pressure profiles of the intergalactic medium. The different approach and classification of the IGM used in their work makes it somewhat difficult to make one-to-one comparisons. However, the temperature profiles from both our works agree in the filamentary core regions, with a short plateau before a steep drop at larger radii. Moreover, they detect higher temperatures for shorter filaments (mentioned in Section 2.4 and described in detail in Galárraga-Espinosa et al. 2020), similarly to results from our high LD filaments. Using the same Illustris-TNG simulation and DisPerSe filament catalogue, Galárraga-Espinosa et al. (2022) analysed the baryon and dark matter densities within filaments. Again, shorter filaments contain higher baryon densities, akin to our high LD filaments. Indeed, our radial profiles agree with their results, with higher densities found at the filament spines, decreasing rapidly to settle at the background level at higher radii. In short, results from two different simulations using two different filament finding methods agree to some extent in the temperature and density profiles. More importantly, both outcomes from simulations agree with observational results presented by Tanimura et al. (2020a).

This Section gave an overview of the results from Papers I and II, describing the thermodynamic properties and spatial distribution of the hot intergalactic medium. Given the high temperatures and low densities of this WHIM, observations of individual gas systems remain scarce. So the question remains, how to detect these missing baryons? The following Section centres on this question, describing the results from Paper III.

3.2 O VII as a tracer of the missing baryons

The aim in Paper III was to derive observational predictions for detecting the missing baryons with X-ray absorption. In particular, we analysed the spatial distribution and column densities of Oxygen and O VII within Bisous filaments. For temperatures at the cores of the high LD filaments ($\log T(K) \sim 6$) and assuming collisional ionisation equilibrium, almost all of the Oxygen has been ionised to O VII. However, as described in Section 1.2.3, ionisation is not driven solely by CIE due to the very low densities in the hot WHIM (see

Figure 3.3 and Figure 6 in Paper III). Thus, O VII constitutes only 30% of the total Oxygen content within the IGM in filaments. However, O VII is still expected to be the dominant ion species at temperatures of $\log T(K) = 5.5 - 7$, especially towards the higher IGM densities.

Given the uncertainties in the ionisation fraction, we studied the spatial densities and distributions both for the Oxygen in general as well as O VII in particular.

3.2.1 Radial density profiles

Since Oxygen in the IGM originates in and is expelled from galaxies, we computed radial number density profiles as a function of distance from the centres of dark matter haloes. For this, we selected haloes within a mass range of $\log M(M_\odot) = 12 - 13.5$, as most of the intergalactic oxygen is expelled from haloes of this mass range. We divided the volume around haloes in concentric, hollow shells, and computed the number density of intergalactic (outside FoF haloes) Oxygen atoms within each shell. We then computed the median value of all the profiles, shown in Figure 1 of Paper III, along with the 68% scatter in the radial profiles. We repeated the process for O VII, noting how, as expected, it remains significantly lower than Oxygen at all radii.

Considering the observational limit of $\log N_{\text{O VII}}(cm^{-2}) = -15$ for the column densities, we derived approximate number density limits of $\log n_{\text{O VII}}(n^{-3}) = -10$ (for a projected path of 10 Mpc) and $\log n_{\text{O VII}}(n^{-3}) = -9$ (a path of 1 Mpc, see Section 2.1.2). In essence, Figure 1 in Paper III indicates the impact parameter from a given central galaxy at which O VII remains detectable. However, the median O VII density does not exceed $\log n_{\text{O VII}}(n^{-3}) = -9$ at any distance from the halo centres. This suggests that filaments crossing the plane of sky perpendicular to the line of sight might not be observable, given the typical filament thickness of one to a few Mpc. For a 10 Mpc long filament aligned with the line of sight, the median O VII number density lingers above the observational limit up to ~ 700 kpc.

In order to estimate the missing baryon content that can be traced with O VII we computed both the hot WHIM and ion density fractions as a function of distance from the nearest halo (Figure 8 in Paper III). The O VII content decreases rapidly with distance, with $\approx 75\%$ of the total O VII mass contained within $3 \times R_{200}$. At the same time, however, the amount of intergalactic hot baryons falls rather steeply as well: $\approx 30\%$ of all the hot WHIM is within $1 - 3 \times R_{200}$ in filaments. While not covering the totality of the missing baryons, this overlap might allow to detect a significant fraction of the missing baryons.

Moreover, the hot WHIM and O VII are not located equally around haloes of different masses, but dominantly surrounding haloes of masses between $\log M_{\text{halo}}(M_\odot) = 12 - 14$ (see Fig. 3.4). Indeed, for haloes within this mass

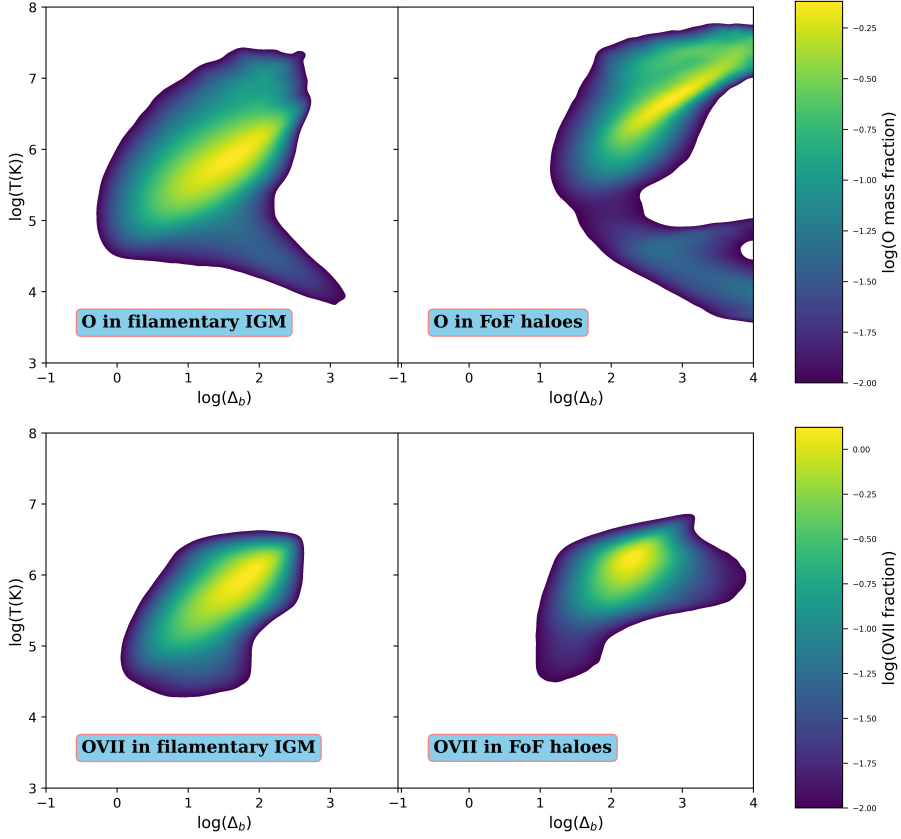


Figure 3.3: Distribution of oxygen (upper panel) and O VII (lower panel) mass as a function of density contrast ($\Delta_b = \rho/\bar{\rho}$) and temperature. The left panels show the oxygen and O VII distributions in the intergalactic medium within Bisous filaments. Gas within filamentary FoF haloes is shown on the right panels. The colour scales indicate the fractions of Oxygen and O VII mass over the total Oxygen and O VII mass in the same environment, respectively (divided by pixel area, values are shown down to 1%). The plots in the lower panel combined are comparable to the results from the Illustris-TNG simulation, shown in the lower middle panel of Figure 2.1.

range, most of the hot WHIM is located within $1 - 3 \times R_{200}$ (or $1 - 2 \times R_{200}$ for the most massive groups). In total, the hot envelopes surrounding haloes of masses between $\log M_{halo}(M_{\odot}) = 12 - 14$ contain $\approx 30\%$ of the hot filamentary WHIM within $1 - 3 \times R_{200}$. This is not a negligible amount; in fact, it accounts for $\approx 7\%$ of all the baryons in EAGLE.

Now the question is, does O VII remain detectable at these radii? To assess this subject, we computed the mass fraction of the hot WHIM in Bisous filaments that is contained within the same volumes as O VII above $\log n_{O\text{VII}}(n^{-3}) = -10$. From all the hot WHIM within filaments, $\approx 27\%$ are spatially collocated within the same volumes as O VII above the aforementioned density limit. This is a similar value to the fraction computed above, albeit slightly smaller. Nonetheless, it means that with future instruments O VII could trace a quarter of the filamentary missing baryons, or $\approx 6\%$ of the total baryon budget.

However, setting the observational limit to the more realistic value of $\log n_{O\text{VII}}(n^{-3}) = -9$, the fraction of hot WHIM traced by O VII reduces to $\approx 7\%$. This corresponds to only $\approx 1\%$ of all the baryons within the EAGLE simulation. Thus, to be detectable, a filament containing hot WHIM and O VII ought to be aligned with the line of sight, with haloes close enough to one another to maintain the ion densities high.

As described in Section 3.1.3, the baryon densities peak along the filament spines, and decrease as a function of distance from the spines. Moreover, the gas temperatures also peak within the central regions of the filaments. Thus, the optimal regions to potentially trace the missing baryons with O VII would be at the cores of filaments, within 1 Mpc from the spines.

In order to explore this assumption, we computed radial profiles of Oxygen number densities for low, medium and high LD filaments (Figure 4 in Paper III). For each distance bin we computed the median Oxygen density within hollow, concentric cylinders. As for the baryon densities and temperatures, the Oxygen number densities peak at the core regions of filament spines, and decrease the further we move from the spines. Moreover, high LD filaments contain higher densities of Oxygen than the rest of the filaments. This is understandable, given that higher LD regions harbour more stars producing Oxygen. Nonetheless, when considering the observational limits described above, the median Oxygen density of even high LD filaments does not reach the level of $\log n_O(cm^{-3}) = -9$. Fortunately, the number densities remain above the optimistic level of $\log n_O(cm^{-3}) = -10$ up to distances of ~ 1 Mpc for both medium and high LD filaments. This would render them observable in the case of a filament aligned along the line of sight, if the majority of Oxygen would be ionised to O VII. As this is not the case, the observational prospects remain arduous.

Truly, the intergalactic Oxygen is more tightly correlated with haloes than filaments (Figure 5 in Paper III). Within 1 Mpc of both haloes and filament

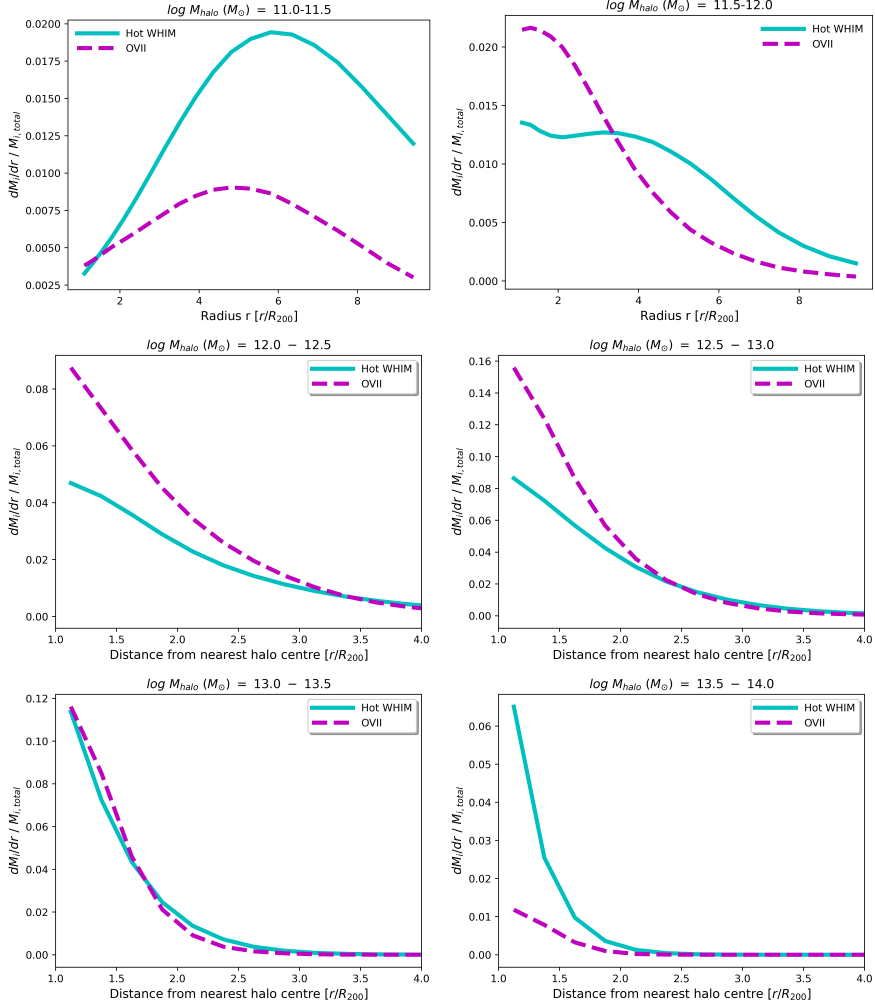


Figure 3.4: Normalised mass fraction of hot WHIM (turquoise line) and O VII (dashed purple line) as a function of distance from the halo centre in units of virial radius R_{200} . Within each distance bin the hot WHIM and O VII mass were divided by the total hot WHIM and O VII in the whole simulation, respectively. Each panel shows the distribution around haloes within six mass bins in the range of $\log M_{\text{halo}} (M_{\odot}) = 11 - 14$.

spines, the Oxygen mass follows a linear relation. As a large fraction of haloes reside within filaments, the Oxygen expelled from said haloes also remains within filaments. However, at larger distances there is a difference. Only $\approx 4\%$ of all the Oxygen mass resides beyond 1.5 Mpc from any given halo, while $\approx 38\%$ of Oxygen can be found further than 1.5 Mpc from the filament spines.

3.2.2 Metal volume fractions and mass distributions within filaments

To further understand how large a fraction of missing baryons could be traced by O VII in observations, it is necessary to study how thoroughly the ions fill the filamentary volumes. To this end we computed the volume covered by the SPH particles containing Oxygen and O VII, respectively (see Figure 2 in Paper III). Since the aim is to produce predictions for observations, we only considered SPH particles with metal or ion densities above $\log n_{O,O\text{VII}}(\text{cm}^{-3}) = -10$ and -9 for a 10 Mpc and a 1 Mpc projection path, respectively. Considering the lower density limit, $\approx 11\%$ and 4% of the total filament volumes are filled with Oxygen and O VII, respectively. For the more realistic limit of $\log n_{O,O\text{VII}}(\text{cm}^{-3}) = -9$, however, the volume filling fraction drops to 1% and 0.4% for Oxygen and O VII, respectively. This is in accordance with the results described in the previous Section. Since the number densities decrease rapidly as a function of distance from the haloes, the metals and ions are unable to properly fill the filamentary volumes.

To comprehend the mass content of Oxygen and O VII within the filaments, we studied their mass distribution as a function of number density (Figure 3 in Paper III). Incidentally, the mass distribution of the intergalactic Oxygen and O VII peak near densities of $\log n_{O,O\text{VII}}(\text{cm}^{-3}) \approx -9$. The fraction of mass contained above this limit corresponds to $\approx 20\%$ of the total mass in the simulation, for both Oxygen and O VII. For the more optimistic limit of $\log n_{O,O\text{VII}}(\text{cm}^{-3}) = -10$, the mass fraction of Oxygen corresponds to $\approx 35\%$ and of O VII to $\approx 45\%$.

Combining the above results we found that a significant fraction of Oxygen and O VII are contained within very small volumes. This, in turn, suggests that the intergalactic Oxygen and O VII are localised in small pockets, in contrast to being distributed throughout the filamentary volumes. This, unfortunately, makes observing O VII all the more challenging.

Notwithstanding, the previous Section shed hope on the use of O VII to trace the hot WHIM: $\approx 7\% - 27\%$ of the hot WHIM within Bisous filaments could be traced by O VII above detectable limits. Corresponding to the immediate surroundings of haloes, this would not include the truly intergalactic regions. Nonetheless, the halo surroundings are rich in hot WHIM, and detecting them would push the observable frontiers well beyond the virial radii of collapsed structures.

These results are the outcome of studying the three-dimensional distribution of gas and ions. In observations, on the other hand, we rely on the two-dimensional projections on the plane of sky. Thus, we created two-dimensional column density maps to study the probabilities to detect an absorbing system in EAGLE. Assuming that the ion quantities are properly simulated, these probabilities can be used as predictions for future X-ray observations.

3.3 O VII column density maps

Having characterised the three-dimensional distribution of O VII within the filamentary IGM, we proceeded to study the observational prospects through column densities (see Section 2.1.2 for a description on how we created the column density maps). As expected by the three-dimensional analysis, the extent of the column densities above the detectable limit of $\log N_{\text{O VII}}(\text{cm}^{-2}) = -15$ does not properly fill the filaments (e.g. Figure 7 in Paper III). Instead, O VII forms isolated islands far from one another.

Nonetheless, the CDDF indicates that above the limit of $\log N_{\text{O VII}}(\text{cm}^{-2}) = -15$, most of the intergalactic O VII absorbers reside within Bisous filaments (Figure 11 in Paper III). Moreover, integrating the CDDF above the limit results in ≈ 4 absorption systems per unit redshift. The caveat here is that the analysis was done for a relatively small box (100 Mpc per side, or $\Delta z \approx 0.02$) and for the simulation snapshot at $z = 0$, without considering the evolution of the filamentary metals. Regardless, this result is in agreement with similar works (e.g. Cen & Ostriker 2006; Branchini et al. 2009; Wijers et al. 2019).

We then proceeded to compute the probability to encounter such absorbers. For this we considered two scenarios, one for the existing filament catalogue done with SDSS galaxies, and another for a future catalogue to be done with 4MOST galaxies. The reason for these two cases comes from the depth of the surveys. The Bisous filament catalogue in SDSS is complete up to redshift $z \approx 0.05$, while 4MOST will reach a comparable completeness up to $z \sim 0.15$. These redshifts correspond to depths of ~ 200 Mpc and ~ 600 Mpc, respectively. Considering the Local Void, the filament catalogue in SDSS is complete only for a radial depth of ≈ 130 Mpc.

The probability of crossing an absorber system was computed by randomly selecting 10 000 lines of sight through EAGLE in random orthogonal directions (X, Y or Z). If a segment with a column density above the detection limit of $\log N_{\text{O VII}}(\text{cm}^{-2}) = -15$ was within a line of sight, it was considered a detection. The difference in depth between EAGLE and SDSS was accounted by adding one random 20 Mpc slice to the line of sight. For the 4MOST sample we continued each line of sight six times through random directions across the box. While this was not an ideal approach, since it did not account for the

cosmic variance or the evolution of the structures, it gave us an estimate of the effect the depth has on the probability to detect an absorber.

The probability to randomly detect an absorbing system, for the SDSS depth of 130 Mpc, is $\approx 11\%$. For the 4MOST depth of 600 Mpc, on the other hand, the probability increases to $\approx 45\%$ (see Figure 12 in Paper III). Thus, 4MOST will greatly improve the probability to encounter an absorber. Subsequently, we studied whether targeting high LD filaments would improve the probability. For this end, we repeated the process described above, but targeting projected areas covered by high LD filaments. As hoped, the probabilities increased up to $\approx 22\%$ and $\approx 50\%$ for SDSS and 4MOST depths, respectively. However, the chances for a bright background source to be behind a high LD filament are somewhat smaller than for a random line of sight, since high LD filaments cover a smaller fraction of the sky. Nonetheless, given the sky coverage and the depth of the 4MOST survey, $\approx 40\%$ of the sky will be covered by a high LD filament. This would suggest that the probability to have a bright AGN behind high LD filaments remains relatively high.

CHAPTER 4

DISCUSSION AND CONCLUSIONS

The two main goals of this doctoral work were to characterise the missing baryons within the large-scale structure of the Universe, and to study the feasibility of using O VII as a tracer of these baryons. This was done with the use of the state-of-the-art hydrodynamic simulation EAGLE. Moreover, we applied two different filament finding methods, Bisous and NEXUS+, to detect the structures of the cosmic web. With the metallicities given directly by the simulation, we implemented ionisation tables obtained from the CLOUDY algorithm to compute the fraction of O VII ions within each simulation particle. We combined these methods and results to draw the conclusions presented in this Chapter.

The baryon content within EAGLE is in agreement with other hydrodynamic simulations (in particular Illustris-TNG), with approximately half of all the baryons residing within cosmic filaments. In Paper I we found that from these filamentary baryons, about a half are in the hot phase of the WHIM, at temperatures of $\log T(K) = 5.5 - 7$. This $\sim 25\%$ of the total baryon budget contains $\approx 79\% - 87\%$ of all the baryons in the hot WHIM within the simulation, depending on the filament finding method used. As the baryons in this phase are hot and diffuse, they have evaded direct detections and are known as the missing baryons.

Another avenue to trace the missing baryons is to use the luminosity of galaxies. As the structure formation is driven by the dark matter, both galaxies and the IGM co-exist within the same large-scale structures. Thus, following the visible galaxy luminosity it is possible to track the invisible IGM. In Paper II we used the EAGLE simulation to derive a scaling relation between the galaxy luminosity and WHIM densities. This relation was then applied to SDSS data to estimate the amount of WHIM baryons (in the temperature range of $\log T(K) = 5 - 7$) within Bisous filaments. This allowed us to compute an estimate for the baryon fraction traced by the LD: $\Omega_{b,LD} \simeq 31\% \pm 10\%$ of the total baryon content.

In EAGLE, the filaments residing in regions with high average LD were found to be more rich in hot WHIM gas. Indeed, radial profiles of these filaments showed higher median temperatures and densities than for the whole sample. The cores of these high LD filaments are optimal for the search of O VII, the dominant ion at $\log T(K) = 5.5 - 7$.

In Paper III we proceeded to study the distribution of O VII ions within Bisous filaments. This was done to assess the probability which next generation X-ray instruments might have for tracing the missing baryons by observing O VII absorption signatures. While it seems that tracing individual

filaments with X-ray absorption will not be feasible for the foreseeable future, next generation instruments might be able to shrink the gap of the missing baryons. The overlap between significant O VII densities and hot WHIM surrounding haloes up to $3 \times R_{200}$ will allow us to tap into a yet undetected reservoir of baryons. Furthermore, the search for missing baryons can neglect the lower mass haloes that are too dim to be easily observed in surveys. In addition, future large galaxy surveys will provide more complete filament catalogues, which can aid in determining redshifts and stacking spectra of background X-ray sources to reveal weaker absorption signals.

Several factors might be the cause for the observational prospects being low. One such factor is the poor distribution of metals into the IGM. Feedback processes might not be powerful enough to fill the filaments at high enough densities. At the same time, only $\approx 33\%$ of the filamentary Oxygen has been ionised to O VII. This explains the significant differences in volume fractions and mass distributions between Oxygen and O VII. While part of the filamentary gas is at too low temperatures for CIE to produce O VII, the low density should allow for warm WHIM to be photoionised to higher ions beyond O VI (the dominant FUV ion at $\log T(K) = 5 - 5.5$). At the same time, however, the low density IGM at higher temperatures allows further photoionisation to even higher ionisation states. This balance between density and temperature, photoionisation and collisional ionisation, plays an important role in the ionisation fractions within the filamentary WHIM.

On the other hand, the results presented here were obtained using a single simulation. While other hydrodynamic simulations seem to agree with most of these results, we are lacking a one-to-one analysis with the same methods across several different simulations. For instance, the SIMBA simulation predicts up to 70% of the baryons to be in the WHIM (Christiansen et al. 2020), with the O VII ions flying further away from the haloes (Bradley et al. 2022). This difference seems to arise from the different feedback methods used in EAGLE and SIMBA, but this would require more thorough investigation. In the case that EAGLE is underestimating the spread of ions into the filament volumes, the results obtained in our work could be treated as conservative lower limits.

Recent works stacking tSZ and X-ray emission maps at the positions of filaments (Tanimura et al. 2020a, 2022), stacking spectra at redshifts from previously known absorption systems (Kovács et al. 2019), as well as fast radio bursts (Macquart et al. 2020) have brought observational evidence of the hot, filamentary WHIM. Nonetheless, individual systems of missing baryons are still waiting to be observed, located within cosmic filaments and traceable with galaxy luminosity density fields. One strategy to detect individual absorbing systems has been to search for X-ray ions at the locations of previously detected FUV ions (e.g. Bonamente et al. 2016; Ahoranta et al. 2020). The scarce number of detections suggest that gases at different temperature phases

might not co-exist at high enough densities for both FUV's and X-rays to be detectable. Thus, instead of using prior absorption signatures to determine the redshifts, an intervening filament detected from large galaxy surveys can be applied. What is more, several intervening filaments along the line of sight can be used to determine a number of potential redshifts for X-ray absorption signals. Shifting an observed spectra at the filament redshifts and stacking at the O VII wavelengths could potentially reveal previously undetected hot WHIM systems.

The veil hiding the missing baryons is finally starting to move aside, revealing the last piece of the puzzle. While the observational prospects of detecting individual O VII absorbers are rather pessimistic, different methods and alternative pathways will lead to ever more detections of the hot WHIM. And this is only the beginning. Once the hot IGM is properly probed, we can begin to understand the interactions and interconnections between collapsed structures, such as galaxies, the circumgalactic and the intra-cluster medium, and the diffuse intergalactic medium feeding into the collapsed structures.

REFERENCES

- Ahoranta, J., Nevalainen, J., Wijers, N., et al. 2020, *Hot WHIM counterparts of FUV O VI absorbers: Evidence in the line-of-sight towards quasar 3C 273*, A&A, 634, A106
- Alam, S., Albareti, F. D., Allende Prieto, C., et al. 2015, *The Eleventh and Twelfth Data Releases of the Sloan Digital Sky Survey: Final Data from SDSS-III*, ApJS, 219, 12
- Aragón Calvo, M. A. 2007, *Morphology and Dynamics of the Cosmic Web*, PhD thesis, University of Groningen
- Aragón-Calvo, M. A., Jones, B. J. T., van de Weygaert, R., & van der Hulst, J. M. 2007, *The multiscale morphology filter: identifying and extracting spatial patterns in the galaxy distribution*, A&A, 474, 315
- Bonamente, M., Nevalainen, J., Tilton, E., et al. 2016, *A possible Chandra and Hubble Space Telescope detection of extragalactic WHIM towards PG 1116+215*, MNRAS, 457, 4236
- Bond, J. R., Kofman, L., & Pogosyan, D. 1996, *How filaments of galaxies are woven into the cosmic web*, Nature, 380, 603
- Bradley, L., Davé, R., Cui, W., Smith, B., & Sorini, D. 2022, *High-ionisation oxygen absorption from the Warm-Hot Intergalactic Medium in Simba*, arXiv e-prints, arXiv:2203.15055
- Branchini, E., Ursino, E., Corsi, A., et al. 2009, *Studying the Warm Hot Intergalactic Medium with Gamma-Ray Bursts*, ApJ, 697, 328
- Cautun, M., van de Weygaert, R., & Jones, B. J. T. 2013, *NEXUS: tracing the cosmic web connection*, MNRAS, 429, 1286
- Cautun, M., van de Weygaert, R., Jones, B. J. T., & Frenk, C. S. 2014, *Evolution of the cosmic web*, MNRAS, 441, 2923
- Cen, R. & Ostriker, J. P. 1999, *Where Are the Baryons?*, ApJ, 514, 1
- Cen, R. & Ostriker, J. P. 2006, *Where Are the Baryons? II. Feedback Effects*, ApJ, 650, 560
- Christiansen, J. F., Davé, R., Sorini, D., & Anglés-Alcázar, D. 2020, *Jet feedback and the photon underproduction crisis in SIMBA*, MNRAS, 499, 2617
- Danforth, C. W., Keeney, B. A., Tilton, E. M., et al. 2016, *An HST/COS Survey of the Low-redshift Intergalactic Medium. I. Survey, Methodology, and Overall Results*, ApJ, 817, 111
- de Jong, R. S., Agertz, O., Berbel, A. A., et al. 2019, *4MOST: Project overview and information for the First Call for Proposals*, The Messenger, 175, 3

- Fang, T., Buote, D. A., Humphrey, P. J., et al. 2010, *Confirmation of X-ray Absorption by Warm-Hot Intergalactic Medium in the Sculptor Wall*, ApJ, 714, 1715
- Ferland, G. J., Korista, K. T., Verner, D. A., et al. 1998, *CLOUDY 90: Numerical Simulation of Plasmas and Their Spectra*, PASP, 110, 761
- Fukugita, M., Hogan, C. J., & Peebles, P. J. E. 1998, *The Cosmic Baryon Budget*, ApJ, 503, 518
- Galárraga-Espinosa, D., Aghanim, N., Langer, M., Gouin, C., & Malavasi, N. 2020, *Populations of filaments from the distribution of galaxies in numerical simulations*, A&A, 641, A173
- Galárraga-Espinosa, D., Aghanim, N., Langer, M., & Tanimura, H. 2021, *Properties of gas phases around cosmic filaments at $z = 0$ in the IllustrisTNG simulation*, A&A, 649, A117
- Galárraga-Espinosa, D., Langer, M., & Aghanim, N. 2022, *Relative distribution of dark matter, gas, and stars around cosmic filaments in the IllustrisTNG simulation*, A&A, 661, A115
- Ganeshaiah Veena, P., Cautun, M., Tempel, E., van de Weygaert, R., & Frenk, C. S. 2019, *The Cosmic Ballet II: spin alignment of galaxies and haloes with large-scale filaments in the EAGLE simulation*, MNRAS, 487, 1607
- Guo, Q., White, S., Angulo, R. E., et al. 2013, *Galaxy formation in WMAP1 and WMAP7 cosmologies*, MNRAS, 428, 1351
- Haardt, F. & Madau, P. 2001, *Modelling the UV/X-ray cosmic background with CUBA*, in *Clusters of Galaxies and the High Redshift Universe Observed in X-rays*, ed. D. M. Neumann & J. T. V. Tran, 64
- Jõeveer, M. & Einasto, J. 1978, *Has the universe the cell structure*, in *IAU Symposium, Vol. 79, Large Scale Structures in the Universe*, ed. M. S. Longair & J. Einasto, 241
- Kaastra, J. S. 2017, *High-resolution X-ray spectroscopy: The coming-of-age*, *Astronomische Nachrichten*, 338, 146
- Kang, H., Ryu, D., Cen, R., & Song, D. 2005, *Shock-heated Gas in the Large-Scale Structure of the Universe*, ApJ, 620, 21
- Kovács, O. E., Bogdán, Á., Smith, R. K., Kraft, R. P., & Forman, W. R. 2019, *Detection of the Missing Baryons toward the Sightline of H1821+643*, ApJ, 872, 83
- Kuutma, T., Poudel, A., Einasto, M., et al. 2020, *Properties of brightest group galaxies in cosmic web filaments*, A&A, 639, A71
- Libeskind, N. I., van de Weygaert, R., Cautun, M., et al. 2018, *Tracing the cosmic web*, MNRAS, 473, 1195
- Liivamägi, L. J., Tempel, E., & Saar, E. 2012, *SDSS DR7 superclusters. The catalogues*, A&A, 539, A80

- Macquart, J. P., Prochaska, J. X., McQuinn, M., et al. 2020, *A census of baryons in the Universe from localized fast radio bursts*, *Nature*, 581, 391
- Malavasi, N., Aghanim, N., Douspis, M., Tanimura, H., & Bonjean, V. 2020, *Characterising filaments in the SDSS volume from the galaxy distribution*, *A&A*, 642, A19
- Mazzotta, P., Mazzitelli, G., Colafrancesco, S., & Vittorio, N. 1998, *Ionization balance for optically thin plasmas: Rate coefficients for all atoms and ions of the elements H to NI*, *A&AS*, 133, 403
- Nelson, D., Kauffmann, G., Pillepich, A., et al. 2017, *The abundance, distribution, and physical nature of highly ionized oxygen OVI, OVII, and OVIII in IllustrisTNG*, *Monthly Notices of the Royal Astronomical Society*, 477
- Nelson, D., Springel, V., Pillepich, A., et al. 2019, *The IllustrisTNG simulations: public data release*, *Computational Astrophysics and Cosmology*, 6, 2
- Nevalainen, J., Tempel, E., Ahoranta, J., et al. 2019, *To be or not to be: the case of the hot WHIM absorption in the blazar PKS 2155-304 sight line*, *A&A*, 621, A88
- Nevalainen, J., Tempel, E., Liivamägi, L. J., et al. 2015, *Missing baryons traced by the galaxy luminosity density in large-scale WHIM filaments*, *A&A*, 583, A142
- Nevalainen, J., Wakker, B., Kaastra, J., et al. 2017, *Discovery of Galactic O iv and O v X-ray absorption due to transition temperature gas in the PKS 2155-304 spectrum*, *A&A*, 605, A47
- Nicastro, F., Fang, T., & Mathur, S. 2022, *Absorption studies of the most diffuse gas in the Large Scale Structure*, arXiv e-prints, arXiv:2203.15666
- Persic, M. & Salucci, P. 1992, *The baryon content of the universe*, *MNRAS*, 258, 14P
- Planck Collaboration, Ade, P. A. R., Aghanim, N., et al. 2014, *Planck 2013 results. I. Overview of products and scientific results*, *A&A*, 571, A1
- Planck Collaboration, Ade, P. A. R., Aghanim, N., et al. 2016a, *Planck 2015 results. XIII. Cosmological parameters*, *A&A*, 594, A13
- Planck Collaboration, Aghanim, N., Arnaud, M., et al. 2016b, *Planck 2015 results. XXII. A map of the thermal Sunyaev-Zeldovich effect*, *A&A*, 594, A22
- Ryu, D., Kang, H., Hallman, E., & Jones, T. W. 2003, *Cosmological Shock Waves and Their Role in the Large-Scale Structure of the Universe*, *ApJ*, 593, 599
- Schaye, J., Crain, R. A., Bower, R. G., et al. 2015, *The EAGLE project: simulating the evolution and assembly of galaxies and their environments*, *MNRAS*, 446, 521
- Shull, J. M., Smith, B. D., & Danforth, C. W. 2012, *The Baryon Census in a Multi-phase Intergalactic Medium: 30% of the Baryons May Still be Missing*, *ApJ*, 759, 23

- Sousbie, T., Pichon, C., & Kawahara, H. 2011, *The persistent cosmic web and its filamentary structure - II. Illustrations*, MNRAS, 414, 384
- Springel, V., White, S. D. M., Jenkins, A., et al. 2005, *Simulations of the formation, evolution and clustering of galaxies and quasars*, Nature, 435, 629
- Stoica, R. S., Martínez, V. J., & Saar, E. 2007, *A three dimensional object point process for detection of cosmic filaments*, Journal of the Royal Statistical Society Series C, 56, 459
- Stoica, R. S., Martínez, V. J., & Saar, E. 2010, *Filaments in observed and mock galaxy catalogues*, A&A, 510, A38
- Tanimura, H., Aghanim, N., Bonjean, V., Malavasi, N., & Douspis, M. 2020a, *Density and temperature of cosmic-web filaments on scales of tens of megaparsecs*, A&A, 637, A41
- Tanimura, H., Aghanim, N., Douspis, M., & Malavasi, N. 2022, *X-ray emission from cosmic web filaments in SRG/eROSITA data*, A&A, 667, A161
- Tanimura, H., Aghanim, N., Kolodzig, A., Douspis, M., & Malavasi, N. 2020b, *First detection of stacked X-ray emission from cosmic web filaments*, A&A, 643, L2
- Tempel, E., Kipper, R., Saar, E., et al. 2014a, *Galaxy filaments as pearl necklaces*, A&A, 572, A8
- Tempel, E., Kipper, R., Tamm, A., et al. 2016a, *Friends-of-friends galaxy group finder with membership refinement. Application to the local Universe*, A&A, 588, A14
- Tempel, E., Stoica, R. S., Kipper, R., & Saar, E. 2016b, *Bisous model-Detecting filamentary patterns in point processes*, Astronomy and Computing, 16, 17
- Tempel, E., Stoica, R. S., Martínez, V. J., et al. 2014b, *Detecting filamentary pattern in the cosmic web: a catalogue of filaments for the SDSS*, MNRAS, 438, 3465
- Tripp, T. M., Lu, L., & Savage, B. D. 1998, *The Relationship between Galaxies and Low-Redshift Weak Ly α Absorbers in the Directions of H1821+643 and PG 1116+215*, ApJ, 508, 200
- Wijers, N. A., Schaye, J., Oppenheimer, B. D., Crain, R. A., & Nicastro, F. 2019, *The abundance and physical properties of O VII and O VIII X-ray absorption systems in the EAGLE simulations*, MNRAS, 488, 2947
- York, D. G., Adelman, J., Anderson, Jr., J. E., et al. 2000, *The Sloan Digital Sky Survey: Technical Summary*, AJ, 120, 1579
- Zappacosta, L., Nicastro, F., Maiolino, R., et al. 2010, *Studying the WHIM Content of Large-scale Structures Along the Line of Sight to H 2356-309*, ApJ, 717, 74
- Zel'dovich, Y. B. 1970, *Gravitational instability: An approximate theory for large density perturbations.*, A&A, 5, 84

SUMMARY IN ESTONIAN

Selle doktoritöö kaks peamist eesmärki olid iseloomustada universumi suuremastaabilise struktuuri raames puuduolevat galaktikavahelist gaasi (st puuduolevaid barüone) ning uurida O VII kasutamise võimalikkust selle gaasi leidmisel. Selleks kasutasime tänapäevast hüdrodünaamilist simulatsiooni EAGLE. Lisaks rakendasime kosmilise võrgustiku struktuurile leidmiseks kahte erinevat filamentide leidmise meetodit, Bisous ja NEXUS+.

Tavalise aine sisaldus EAGLE-s on kooskõlas teiste hüdrodünaamiliste simulatsioonidega, kusjuures umbes pooled barüonidest asuvad kosmilistes filamentides. Leidsime, et umbes pool filamentide gaasist on kuum galaktikatevaheline keskkond (WHIM), mille temperatuur on $\log T(K) = 5.5 - 7$. See umbes 25% tavalise aine koguhulgast sisaldab omakorda $\approx 79\% - 87\%$ kogu puuduolevast galaktikavahelist gaasist. Kuna selles faasis olev gaas on kuum ja hajus, pole seda otsese meetoditega senimaani avastatud.

Teine võimalus puuduoleva gaasi leidmiseks on kasutada galaktikate heledust. Kuna Universumi struktuuride moodustumist juhib tume aine, eksisteerivad nii galaktikad kui ka galaktikatevaheline keskkond üheskoos samades suuremastaabilise struktuuri elementides. Seega, jälgides vaadeldavat galaktikate heledust, on võimalik jälgida ka nähtamatut galaktikatevahelist ainet. Galaktikate heleduse ja WHIM-i tiheduse vahelise seose leidsime EAGLE simulatsiooni andmete alusel. Seejärel rakendasime saadud seost SDSSi andmetele, et hinnata WHIM-i kogust Bisous filamentides. See võimaldas meil hinnata galaktikavahelise gaasi osakaalu, mis vastab heledustihedusele (LD): $\Omega_{b,LD} \simeq 31\% \pm 10\%$ kogu tavalise aine osakaalust (ei sisalda tumeainet). EAGLE-st leidsime, et filamendid, mis asuvad suure heledustiheduse LD piirkondades, on rikkad ka kuuma WHIM-i gaasi poolest. Nende filamentide radiaaljaotustes esineb tõepoolest kogu valimiga võrreldes kõrgemaid keskmisi temperatuure ja tihedusi. Suure LD-ga filamentide südamikud on ideaalne koht, kust otsida O VII ioone temperatuuriga $\log T(K) = 5.5 - 7$.

Seejärel uurisime O VII ioonide jaotust Bisousi filamentides. Kasutades simulatsioonis saadud metallilisuseid ja CLOUDY algoritmist saadud ionisatsiooni tabeleid, arvutasime iga simulatsiooni osakese jaoks O VII ioonide osakaalu. Et hinnata, kui tõenäoliselt on järgmise põlvkonna röntgenteleskoobid võimelised puuduva barüone detekteerima, uurisime nii filamentide O VII kahemõõtmelisi pindtihedusi kui ka kolmemõõtmelisi arvutihedusi. Saime, et O VII tihedused on liiga väikesed, et neid korrektselt tuvastada. Seega, gaasi leidmine üksikutes filamentides röntgenkiirguse neeldumise abil ei ole lähitulevikus võimalik, ning O VII ei ole kasutatav kogu puuduva barüonide leidmiseks. Kuid tulevase röntgenteleskoobi abil on võimalik vaadelda märkimisväärt osa sellest, valgustades üht osa seni veel vaatlemata universumist.

ACKNOWLEDGEMENTS

The research presented in this Thesis has been financially supported by the Estonian Research Council grants (PUT246, IUT40-2 and PRG1006) and the Centre of Excellence “Dark side of the Universe” (TK133), financed by the European Regional Development Fund.

I always felt as if these acknowledgements and thanks were a compulsory duty, an ending without real substance. But now that I am in this position, I feel the strength and meaning this ritual entails. To be able, even if briefly, to thank all those who helped and journeyed with me through the adventure that doing a PhD is.

My first and foremost gratitude goes to my supervisor, Jukka. Thank you for your patience and guidance, and for teaching me how to live in the world of science. And also thank you for all the memorable work trips and good times outside of work. Following your example, I will demand quality from my work and integrity from myself, without forgetting the artistic side of life. Kiitos!

Many thanks to all the people at Tartu Observatory, you make it a very special place. Going to the observatory was always a pleasure, and something to look forward during the pandemic. I am especially grateful to everyone in the cosmology department, Antti, Elmo, Maret, Rain, Jaan Einasto, Peeter, Taavi, Juhan, Enn, Indrek, Shishir and María. You have inspired me and I have learned so much from all of you. Please keep up with the astronomy sauna!

I would also like to thank Pekka, for all your advice and help in the work presented in this thesis. Kiitos, kun sain olla sinun vuokralaisena, ja kiitos tieteen täytteisistä saunailloista ja öisistä kendo otteluista.

A very special thank you to Heidi, without you I would have never started my PhD in Tartu. And thank you Max, for being part of my scientific work and your hospitality in Huntsville, Alabama. Nastasha, thank you for all your invaluable help.

A wholehearted thank you to all my fellow PhD students. Teet, Maarja, Punya, Daniel, Moorits, you were there since the beginning, and helped me so much with all the challenges of starting a PhD in a new country. With you, working at the observatory did not feel like working at all. And I will always remember with fondness all the laughs and tears, nights out, days in, holidays spent together in the countryside, music festivals, in short, the good times. Most of you have already finished your PhD's and are now living the life of a scientist. I am glad to be joining the club. Lets keep in touch, both academically and socially! Kate, Jad and Mousumi, you came towards the end, but I already feel as if I have known you forever. I am glad I had the chance to meet you and spend time with you, we will surely meet again many times!

I wish to thank Heleri, Ayush and Saimoon. I feel like we became friends instantly, from the very first moment we met. The bus rides to Tõravere and back became a highlight of the day thanks to you. Thank you Jan, Jaan Laur, Mait, Helen and Kairi, the observatory band will always have a special place in my heart. Keep on rocking!

A heartfelt thank you to all my friends from outside the observatory. Karl and Priit, my life in Estonia would not have been the same without you, thank you. Nisa, gracias por todos los buenos momentos y las risas, y por devolver un poco de las islas Canarias a mi vida. Y Leonor, te deseo todo lo mejor, espero que algún día leas esto. Thank you Suraj, I really miss the months we lived in Eha, I am glad we spent that time together. Jessie, merci beaucoup. Sarah, Charlotte and Charlie, thank you for all the great parties and memorable times, and for showing me that other, art-filled universe.

I should not forget my friends from the past, who stayed with me during this whole time virtually (with the occasional visits), thank you. Thank you people in Joonas' Universe, for all the great discussions and idle talks that gave me the necessary breaks from the scientific work. Thank you, Jussi, despite our scientific paths diverging, we never moved away from one another. And thank you Manuel and Carla, for always being there despite the distance in space and time.

The Tartu kendo club deserves a special mention as well. The physical and mental exercise required in kendo was the perfect balance to sitting behind a desk all day. Thank you Margus, for all these years of good keiko.

A big thank you goes to Barlova and its people, especially Elina, Rivo, Simone and Hanna. Having that living room outside of home made my stay in Tartu all the more enjoyable. Suur aitäh, one day I will definitely come back for a Must Nunn!

I wish to thank my parents, Jorma and Ulla, for letting me follow the path my heart craved for, without ever doubting me. And for all the support throughout my studies, spiced with occasional tips and good advice. Thank you Tuuli, my little sister, for always being there, even when you were (literally!) on the other side of this blue planet. The winter/spring we spent together in Kostila was unforgettable!

A big thank you to my other family, Masatoshi, Natsuko and Rika. Thank you for accepting me as I am, and always being curious to what I do. ありがとうございます! And thank you, Yohei, for the past summer, I look forward to spending more time with you!

Last but definitely not least, I am eternally grateful to my beloved wife, Haruka. Your full support and unconditional love mean the world to me. Despite the hardships and sacrifices that living between two (or three) countries brought you, you never complained or criticised, even once, this decision of mine to follow my dream. Truly, sincerely, thank you, kiitos, ありがとう.

PUBLICATIONS

CURRICULUM VITAE

Personal data

Name	Toni Tuominen
Date and place of birth	5 October 1988, Helsinki, Finland
Citizenship	Finnish
Current employment	Institut d’Astrophysique Spatiale
Address	IAS, Université Paris Saclay Bât 120 – 121 rue Jean Teillac 91405 ORSAY CEDEX, FRANCE
Phone	(+372) 5676 6122
E-mail	toni.tuominen@universite-paris-saclay.fr

Education

1994 – 2006	Colegio Casa Azul
2006 – 2016	University of Turku, undergraduate student, BSc 2016 (Physics)
2016 – 2017	University of Turku, graduate student, MSc 2017 (Astronomy)
2017 –	University of Tartu, PhD student

Professional training

June 2019	Summer school “CSC Summer School in High-performance computing”, Nuukio, Finland.
-----------	---

Conference presentations

September 2017	Conference “Tartu–Tuorla annual meeting 2017: What matters”, Tartu, Estonia.
June 2018	Conference “WHIM and Cluster Outskirts: Lost and Found Baryons in the Local Universe”, Alabama, USA
October 2018	Conference “Tartu–Tuorla cosmology conference 2018: The large scale properties of the universe as a whole”, Kaarina, Finland
February 2019	Conference “Tartu–Tuorla cosmology conference 2019: Einasto’s profile”, Tartu, Estonia

June 2019	Conference “XMM-NEWTON 2019 science workshop: Astrophysics of Hot Plasma in Extended X-Ray Sources”, Madrid, Spain
June 2020	Conference “Tartu-Orsay Workshop 2020”, Tartu, Estonia
March 2021	Conference “Physics Days 2021”, Jyväskylä, Finland (online)
October 2021	Conference “Tartu–Tuorla cosmology conference 2021: Interaction of the cosmic matter”, Turku, Finland
March 2022	Conference “Cosmic Cartography 2022: Exploring the Cosmic Web and Large-Scale Structure”, Kashiwa, Japan (online)
May 2022	Conference “Tartu–Tuorla cosmology conference 2022: Galaxy dynamics and beyond”, Laulasmaa, Estonia
June-July 2022	Conference “European Astronomical Society annual meeting 2022”, Valencia, Spain

Language skills

Finnish	first language
English	fluent
Spanish	fluent
Estonian	intermediate
Japanese	intermediate

Honours and Awards

2021	E. Öpik stipend (Tartu Observatory)
------	-------------------------------------

Fields of research

Large scale structure of the universe,
galaxy evolution in cosmic filaments,
N-body cosmological simulations.

Publications

1. **Tuominen, T.**, Nevalainen, J., Heinämäki, P., Tempel, E., Wijers, N., Bonamente, M., Aragon-Calvo, M.A., Finoguenov, A., *Cosmic metal invaders: intergalactic O VII as a tracer of the hot WHIM within cosmic filaments in the EAGLE simulation*, Astronomy & Astrophysics, accepted for publication

2. Holt, P., **Tuominen, T.**, Nevalainen, J., Bonamente, M., Kuutma, T., Heinämäki, P., Tempel, E., 2022, *The scaling relation between galaxy luminosity and WHIM density from EAGLE simulations with application to SDSS data*, Monthly Notices of the Royal Astronomical Society, 513
3. **Tuominen, T.**, Nevalainen, J., Tempel, E., Kuutma, T., Wijers, N., Schaye, J., Heinämäki, P., Bonamente, M., Ganeshiah Veena, P., 2021, *An EAGLE view of the missing baryons*, Astronomy & Astrophysics, 646
4. Nilsson, K., Lindfors, E., Takalo, L. O., Reinthal, R., Berdyugin, A., Sillanpää, A., Ciprini, S., Halkola, A., Heinämäki, P., Hovatta, T., Kadenius, V., Nurmi, P., Ostorero, L., Pasanen, M., Rekola, R., Saarinen, J., Sainio, J., **Tuominen, T.**, Villforth, C., Vornanen, T., Zaprudin, B., 2018, *Long-term optical monitoring of TeV emitting blazars. I. Data analysis*, Astronomy & Astrophysics, 620
5. Sandrinelli, A., Covino, S., Treves, A., Lindfors, E., Raiteri, C. M., Nilsson, K., Takalo, L. O., Reinthal, R., Berdyugin, A., Fallah Ramazani, V., Kadenius, V., **Tuominen, T.**, Kehusmaa, P., Bachev, R., Strigachev, A., 2017, *Gamma-ray and optical oscillations of 0716+714, MRK 421, and BL Lacertae*, Astronomy & Astrophysics, 600
6. The MAGIC Collaboration and Bogosavljevic, M., Ioannou, Z., Mauche, C.W., Palaologou, E.V., Pérez-Torres, M. A., **Tuominen, T.**, 2014, *MAGIC search for VHE γ -ray emission from AE Aquarii in a multiwavelength context*, Astronomy & Astrophysics, 568
7. Lopez-Coto, R., Blanch Bigas, O., Cortina, J., Hadasch, D., Takalo, L., Torres, D., Bogosavljevic, M., Ioannou, Z., Mauche, C. W., Palaologou, E. V., Perez-Torres, M. A., **Tuominen, T.**, 2013, *Search for TeV γ -ray emission from AE Aqr coincident with high optical and X-ray states with the MAGIC telescopes*, arXiv:1309.2503

ELULOOKIRJELDUS

Isikuandmed

Nimi	Toni Tuominen
Sünniaeg ja +koht	5 Oktoober 1988, Helsinki, Soome
Kodakondsus	soome
Praegune töökoht	Institut d'Astrophysique Spatiale
Aadress	IAS, Université Paris Saclay Bât 120 – 121 rue Jean Teillac 91405 ORSAY CEDEX, FRANCE
Telefon	(+372) 5676 6122
E-mail	toni.tuominen@universite-paris-saclay.fr

Haridus

1994 – 2006	Colegio Casa Azul
2006 – 2016	Turku Ülikool, üliõpilane, BSc 2016 (füüsika)
2016 – 2017	Turku Ülikool, magistrant, MSc 2017 (füüsika)
2017 –	Tartu Ülikool, doktorant

Täiendkoolitus

Juuni 2019	Suvekool “CSC Summer School in High-performance computing”, Nuuksio, Soome.
------------	---

Konverentside ettekanded

September 2017	Konverents “Tartu–Tuorla annual meeting 2017: What matters” Tartu, Eesti
Juuni 2018	Konverents “WHIM and Cluster Outskirts: Lost and Found Baryons in the Local Universe” Alabama, USA
Oktoober 2018	Konverents “Tartu–Tuorla cosmology conference 2018: The large scale properties of the universe as a whole”, Kaarina, Soome
Veebruar 2019	Konverents “Tartu–Tuorla cosmology conference 2019: Einasto’s profile”, Tartu, Eesti

Juuni 2019	Konverents “XMM-NEWTON 2019 science workshop: Astrophysics of Hot Plasma in Extended X-Ray Sources”, Madrid, Hispaania
Juuni 2020	Konverents “Tartu–Orsay Workshop 2020”, Tartu, Eesti
Märts 2021	Konverents “Physics Days 2021” Jyväskylä, Soome (online)
Oktoober 2021	Konverents “Tartu–Tuorla cosmology conference 2021: Interaction of the cosmic matter”, Turku, Soome
Märts 2022	Konverents “Cosmic Cartography 2022: Exploring the Cosmic Web and Large-Scale Structure”, Kashiwa, Jaapan (online)
Mai 2022	Konverents “Tartu–Tuorla cosmology conference 2022: Galaxy dynamics and beyond”, Laulasmaa, Eesti
Juuni-Juuli 2022	Konverents “European Astronomical Society annual meeting 2022”, Valencia, Hispaania

Keelteoskus

soome keel	emakeel
inglise keel	väga hea
hispaania keel	väga hea
eesti keel	madal kesktase
jaapani keel	madal kesktase

Autasud ja stipendiumid

2021	E. Öpik stipendium (Tartu Observatoorium)
------	---

Peamised uurimissuunad

Universumi suuremastaabiline struktuur,
galaktikate evolutsioon kosmilistes filamentides,
simulatsioonid.

DISSERTATIONES ASTRONOMIAE UNIVERSITATIS TARTUENSIS

1. **Tõnu Viik.** Numerical realizations of analytical methods in theory of radiative transfer. Tartu, 1991.
2. **Enn Saar.** Geometry of the large scale structure of the Universe. Tartu, 1991.
3. **Maret Einasto.** Morphological and luminosity segregation of galaxies. Tartu, 1991.
4. **Urmas Haud.** Dark Matter in galaxies. Tartu, 1991.
5. **Eugene A. Ustinov.** Inverse problems of radiative transfer in sounding of planetary atmospheres. Tartu, 1992.
6. **Peeter Tenjes.** Models of regular galaxies. Tartu, 1993.
7. **Ivar Suisalu.** Simulation of the evolution of large scale structure elements with adaptive multigrid method. Tartu, 1995.
8. **Teimuraz Shvelidze.** Automated quantitative spectral classification of stars by means of objective prism spectra: the method and applications. Tartu, 1999.
9. **Jelena Gerškevič.** Formation and evolution of binary systems with compact objects. Tartu, 2002.
10. **Ivan Suhhonenko.** Large-scale motions in the universe. Tartu, 2003.
11. **Antti Tamm.** Structure of distant disk galaxies. Tartu, 2006.
12. **Vladislav-Veniamin Pustynski.** Modeling the reflection effect in pre-cataclysmic binary systems. Tartu, 2007.
13. **Anna Aret.** Evolutionary separation of mercury isotopes in atmospheres of chemically peculiar stars. Tartu, 2009.
14. **Mari Burmeister.** Characteristics of the hot components of symbiotic stars. Tartu, 2010.
15. **Elmo Tempel.** Tracing galaxy evolution by their present-day luminosity function. Tartu, 2011.
16. **Anti Hirv.** Estimation of time delays from light curves of gravitationally lensed quasars. Tartu, 2011.
17. **Rain Kipper.** Galaxy modelling: dynamical methods and applications. Tartu, 2016, 134 p.
18. **Lauri Juhan Liivamägi.** Properties and spatial distribution of galaxy superclusters. Tartu, 2017, 185 p.
19. **Jaan Laur.** Variability survey of massive stars in Milky Way star clusters. Tartu, 2017, 183 p.
20. **Boris Zhivkov Deshev.** On the coevolution of galaxies and their host clusters. Tartu, 2019, 199 p.
21. **Tiina Liimets.** Nebulosities and jets from outbursting evolved stars. Tartu, 2019, 207 p.
22. **Maarja Bussov.** Clustering Analysis for Astrophysical Structures. Tartu, 2020, 113 p.
23. **Teet Kuutma.** Galaxies and non-galactic baryons in cosmic filaments. Tartu, 2021, 123 p.